Journal of Nanobiotechnology

RESEARCH Open Access

Enhanced osteogenic differentiation in 3D hydrogel scaffold via macrophage mitochondrial transfer

Shui Qiu[1†], Lili Cao[2†], Dingding Xiang[3], Shu Wang[3], Di Wang[3], Yiyi Qian[3], Xiaohua Li[4] and Xiaoshu Zhou[1*]

Abstract

To assess the efficacy of a novel 3D biomimetic hydrogel scaffold with immunomodulatory properties in promoting fracture healing. Immunomodulatory scaffolds were used in cell experiments, osteotomy mice treatment, and single-cell transcriptomic sequencing. In vitro, fluorescence tracing examined macrophage mitochondrial transfer and osteogenic differentiation of bone marrow-derived mesenchymal stem cells (BMSCs). Scaffold efficacy was assessed through alkaline phosphatase (ALP), Alizarin Red S (ARS) staining, and in vivo experiments. The scaffold demonstrated excellent biocompatibility and antioxidant-immune regulation. Single-cell sequencing revealed a shift in macrophage distribution towards the M2 phenotype. In vitro experiments showed that macrophage mitochondria promoted BMSCs' osteogenic differentiation. In vivo experiments confirmed accelerated fracture healing. The GAD/Ag-pIO scaffold enhances osteogenic differentiation and fracture healing through immunomodulation and promotion of macrophage mitochondrial transfer.

Keywords Fracture healing, 3D biomimetic hydrogel scaffold, Macrophage mitochondrial transfer, Immunomodulation, Macrophage subpopulation, Bone marrow mesenchymal stem cells, Osteogenic differentiation

Background

Fracture is a common orthopedic condition that not only affects the quality of life of patients but can also lead to serious complications [1, 2]. Restoring the normal structure and function of the fractured bone is crucial for the patient's recovery [3–5]. Currently, the treatment methods for fracture healing include surgical realignment and fixation. Traditional approaches to fracture treatment have limitations such as postoperative infections, incomplete bone healing, and risks of re-fracture [6–8]. Moreover, in certain circumstances, such as in the elderly or patients with chronic diseases, the fracture healing process may present significant difficulties and delays [9–11]. Thus, the search for a novel therapeutic strategy capable of promoting fracture healing is of paramount importance [12–14].

Bone marrow-derived mesenchymal stem cells (BMSCs) are a type of multipotent stem cells originating from the bone marrow, and their key role in fracture healing has been demonstrated [15–17]. BMSCs possess osteogenic potential and can differentiate into osteoblasts, promoting the generation of new bone [18, 19].

†Shui Qiu and Lili Cao regarded as co-first authors.

*Correspondence:
Xiaoshu Zhou
13889291613@163.com
[1]Department of Orthopedics, First Hospital of China Medical University, No. 155 Nanjing North Street, Shenyang, Liaoning Province, China
[2]Department of Medical Oncology, First Hospital of China Medical University, No. 155 Nanjing North Street, Shenyang, China
[3]School of Mechanical Engineering and Automation, Foshan Graduate School of Innovation, Northeastern University, Shenyang 110819, China
[4]Department of Orthopedics, Zhongmeng Hospital, Arong Banner, Hulunbuir City, Inner, Mongolia

Hence, exploring novel strategies to promote BMSCs' osteogenic differentiation holds significant significance.

Macrophages, as immune cells, play a vital role in the fracture healing process [20–22]. Recent studies have indicated that macrophages regulate the osteogenic differentiation of stem cells by modulating their mitochondrial function [23, 24]. Mitochondria are intracellular organelles responsible for synthesizing the energy required by cells and participating in various essential cellular metabolic processes [25–27]. Therefore, regulating the process of macrophage mitochondrial transfer may contribute to promoting BMSCs' osteogenic differentiation and thus facilitate fracture healing.

Hydrogels, as porous, highly water-absorbent, and biocompatible materials, have demonstrated significant potential in various fields such as tissue engineering, drug delivery, and cell culture [28–30]. Inspired by mussels, dopamine (DA) is considered a promising antioxidant that can reduce oxidative stress by clearing reactive oxygen species (ROS) and downregulating inflammatory mediators [31, 32]. Iron ions play a crucial role in the process of bone mineralization, influencing the formation and deposition of calcium-phosphate in bones. They regulate the transformation of mineral precursors and mineral formation, thereby promoting mineralization and hardening of bone tissue, while silver nanoparticles confer antibacterial activity to scaffolds by releasing silver ions and generating ROS to attack multiple bacterial targets [33].

This study aims to investigate the potential application of an immunomodulatory 3D biohydrogel scaffold in the treatment of bone fractures. We report the development of a 3D biohydrogel scaffold (GAD/Ag-pIOPNs) using iron oxide-dopamine-silver nanoparticles (Ag-pIOPNs) as the material, demonstrating immunomodulatory properties [34–36]. The GAD/Ag-pIOPNs scaffold treatment significantly alters the subpopulation distribution of macrophages, promotes the polarization of M2 macrophages, and enhances the osteogenic differentiation of BMSCs, thereby expediting the bone healing process in mice.

Through our research, we aim to elucidate the promoting effect of the immunomodulatory 3D biomimetic hydrogel scaffold on macrophage mitochondrial transfer, as well as its impact on BMSCs' osteogenic differentiation and fracture healing. Our study will provide new therapeutic strategies for fracture treatment, with the potential to enhance bone defect repair and patient recovery. Additionally, our research will contribute to a deeper understanding of the reciprocal regulatory mechanisms between macrophages and BMSCs and provide scientific evidence for the development of other related treatment approaches.

Results and discussion

Preparation and characterization of dopamine-modified Alg/Ag-pIOPNs hydrogel

Initially, we prepared GAD/Ag-pIO hydrogels in vitro. The preparation process and reaction mechanism of the Ag-pIOPNs are detailed in Fig. S1. The schematic diagram of the preparation of 3D-printed hydrogels (GAD/Ag-pIO) using Ag-pIOPNs as functional components is illustrated in Fig. 1.

The morphology and particle size of the nanoparticles were characterized using a Transmission Electron Microscope (TEM). The diameter of IOPNs was approximately 20 nm (Fig. S2A). The dopamine-modified IOPNs (pIOPNs) exhibited a typical core-shell structure, with the shell layer on the surface confirming the successful modification by dopamine molecules (Fig. S2B). The presence of spherical particles on the surface of pIOPNs demonstrated the in-situ growth of silver nanoparticles (Fig. S2C). The hydrated particle size of the nanoparticles was determined, showing a slight increase from IOPNs to Ag-pIOPNs, with a particle size ranging from 40 to 50 nm (Fig. S2D). Zeta potential measurements revealed a change in the surface charge from positive to negative after dopamine modification, with the Zeta potential of pIOPNs decreasing from 35 mV to -7.6 mV. This change indicated the ionization of phenolic hydroxyl groups by dopamine, and the Zeta potential of Ag-pIOPNs approached neutrality (Fig. S2E). The loading capacity of dopamine on Ag-pIOPNs was analyzed by thermogravimetric analysis (TG), which showed distinct stages of water evaporation below 100 °C, dopamine decomposition between 100 °C and 300 °C, and dopamine degradation at 400 °C. Based on the weight loss, the loading capacity of dopamine in Ag-pIOPNs was determined to be 8.7%, and the loading capacity of silver was 9.2% (Fig. S2F), confirming the successful preparation of Ag-pIOPNs nanoparticles.

Elemental analysis revealed the presence of Ag, N, and Fe in the Gel/AlgDA hydrogel scaffold (GAD/Ag-pIO), suggesting uniform incorporation of GAD/Ag-pIO (Fig. 2A). Upon addition of GAD/Ag-pIO, the sol-gel transition behavior of the hydrogel was enhanced (Fig. 2B). The compression modulus data indicated that with increasing Ag-pIOPNs content, the gel's compressive strength improved significantly, reaching nearly a four-fold increase at 10 wt% Ag-pIOPNs (Fig. 2C). Furthermore, the swelling capability of the hydrogel initially increased and then decreased with the addition of Ag-pIOPNs (Fig. 2D). As Ag-pIOPNs were added, the porosity of the hydrogel decreased, leading to a denser gel structure (Fig. 2E). Optimal porosity and water retention are vital for cell migration and growth; thus, further investigations will focus on incorporating 5 wt% Ag-pIOPNs for in-depth research.

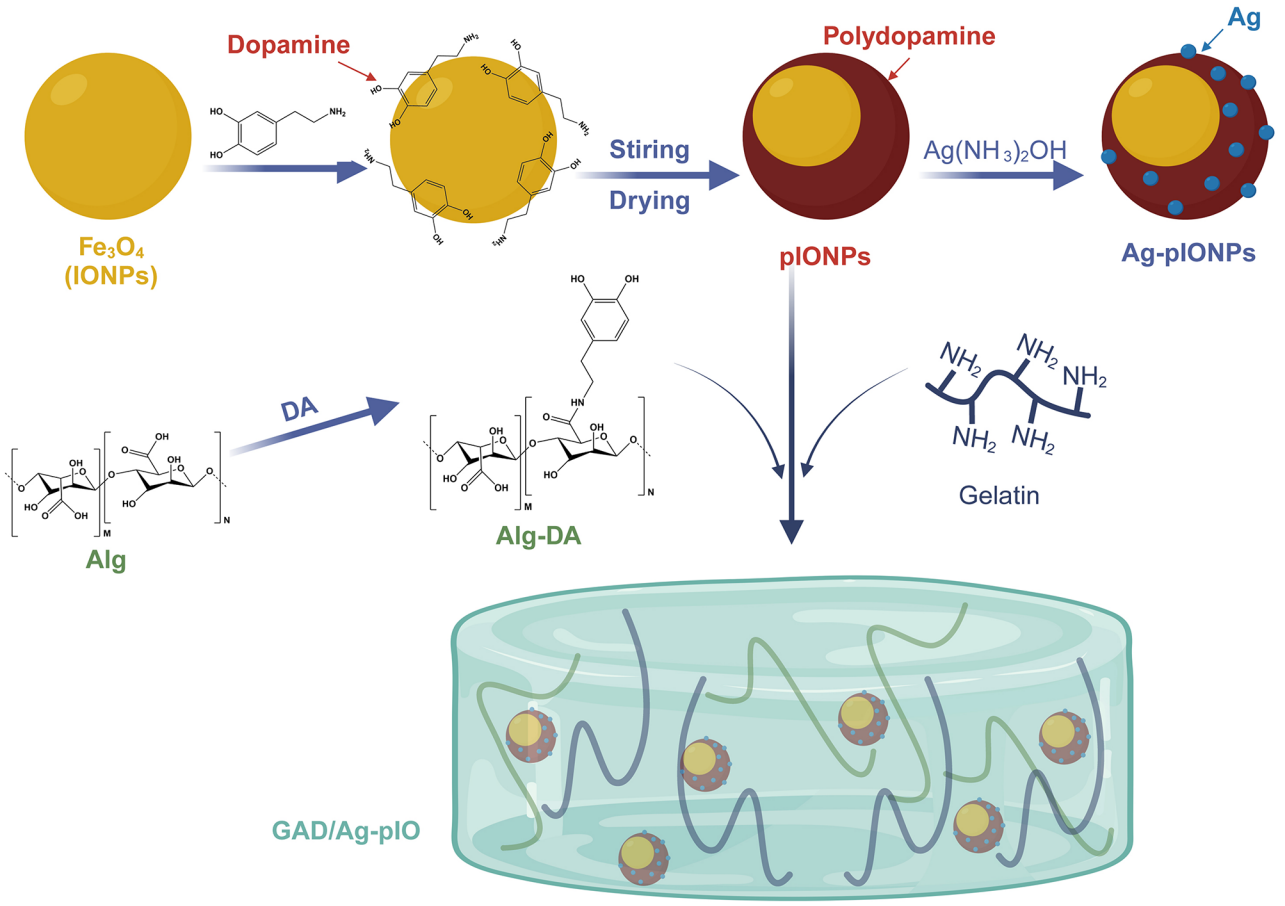

Fig. 1 Schematic diagram illustrating the preparation of GAD/Ag-pIO hydrogel

Rheological and mechanical properties analysis of composite hydrogels

To evaluate the printability and mechanical properties of the composite hydrogel, we initially conducted a rheological analysis. Shear rate measurements were employed to assess viscosity, revealing that all groups exhibited shear-thinning behavior, confirming the hydrogel's suitability as an extrudable material (Fig. 3A). The reduction in the Gel/Alg-DA ratio resulted in an increase in G′ values, indicating an enhancement in the hydrogel's stiffness (Fig. 3B). The G100A0 group displayed the lowest average compressive strength, which increased as the Gel/Alg-DA ratio decreased (Fig. 3C). The gel-to-gel transition temperatures (Ttrans) for the four groups were all around 31 °C, with no influence on the printing temperature at room temperature when additional components were added (Fig. S3). Gels under the G100A0, G90A10, G80A20, and G70A30 ratios exhibited uniform extrusion at conditions of 170/15, 220/12, 280/12, and 360/15 (kPa/mms-1) (Fig. 3D). With an increase in Alg-DA content, the viscosity of the hydrogel increased, along with the required extrusion pressure. By systematically optimizing parameters, successful 3D printing was achieved for all four gel ratios (Fig. 3E). As the Gel/Alg-DA ratio decreased, the micro-porosity of the hydrogel diminished (Fig. 3F). We conducted a 4-week degradation assessment of the printed scaffolds in PBS, followed by weighing freeze-dried samples to determine the post-degradation gel mass (Fig. 3G). The results indicated that an increase in the Alg-DA ratio led to more dynamic cross-linking points and a slower degradation rate. Consequently, the primary component ratio for the final gel was determined to be Gel/Alg-DA=70/30 through preselecting the composition ratios.

Silver ions possess antibacterial properties, and their release is a synergistic oxidation process. Alongside degradation experiments, we measured the release of silver ions (Ag^+) from Gel/Alg-DA=70/30 with 5 wt% Ag-pIOPNs scaffolds. The scaffold exhibited a relatively high non-cumulative silver ion concentration on the first day (5.12 mg/L), gradually decreasing to 1.78 mg/L thereafter. By the 9th day, the cumulative concentration of released Ag+from the scaffold reached 14.3 mg/L (Fig. 3H). Previous studies have shown that silver ion concentrations in the range of 10–100 mg/L can inhibit bacterial growth without compromising biocompatibility

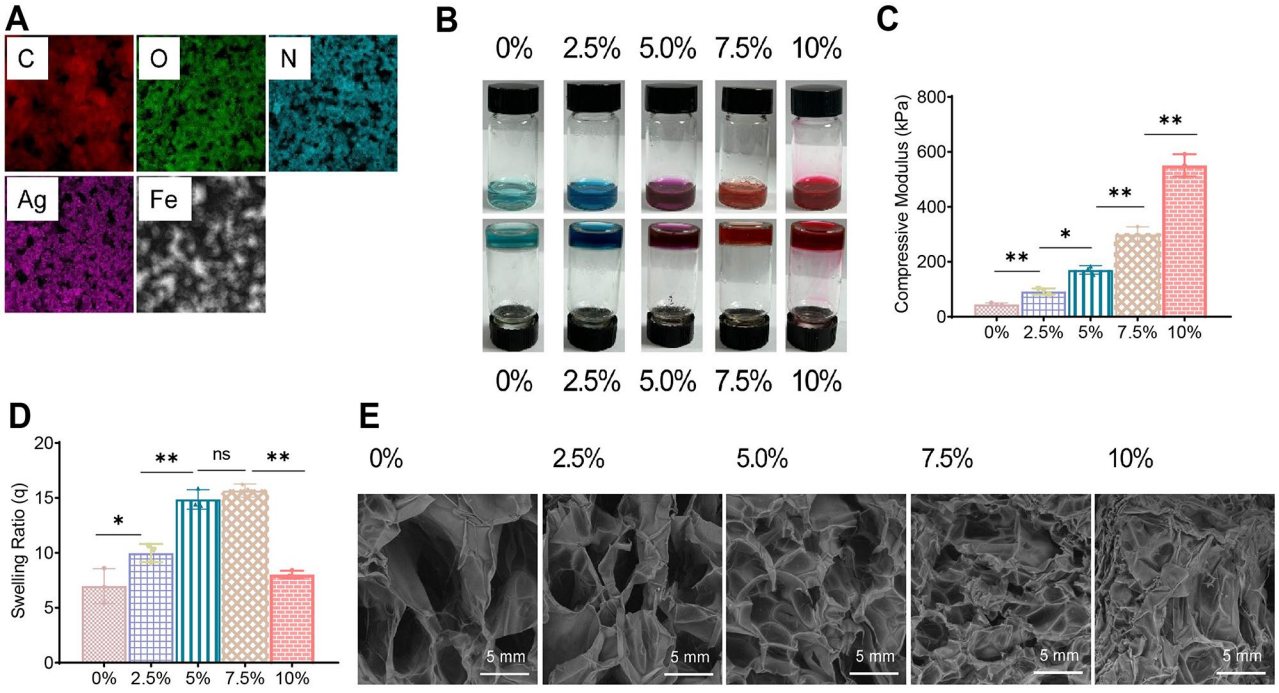

Fig. 2 Characterization of GAD/Ag-pIO hydrogel *Note* (**A**) EDS image of GAD/Ag-pIO; (**B**) Sol-gel transition diagram of GAD/Ag-pIO hydrogel with different concentrations; (**C**) Compression modulus graph of GAD/Ag-pIO; (**D**) Swelling rate measurement graph of GAD/Ag-pIO hydrogel; (**E**) SEM observation image of freeze-dried GAD/Ag-pIO gel, scale = 5 mm. The experiment was repeated three times; ns indicates no significant difference, *$P < 0.05$ indicates significance, and ** indicates $P < 0.01$

[37]. BMDM cells were isolated from murine bone marrow (Fig. S4). Following a 24-hour culture, the viability of BMDMs in the GAD/Ag-pIO group was 98.95 ± 1.02%, comparable to the GA group (97.22 ± 3.05%) and the control group (97.02 ± 1.39%) (Fig. S5A-B). The proliferation of BMDMs in the GAD/Ag-pIO group from day 1 to day 5 showed no significant difference compared to the GA and control groups (Fig. S5C).

In conclusion, we successfully prepared a 3D-printed GAD/Ag-pIO scaffold with good mechanical properties and suitable degradation performance. It provides a microenvironment conducive to cell growth and can be utilized for fracture implant therapy.

Regulation and clearance effects of GAD/Ag-pIO scaffold on early inflammatory response and ROS in fracture healing

During the initial phase of the inflammatory response in fracture healing, a significant amount of ROS is generated to regulate inflammation. However, excessive ROS can be detrimental to cells. Therefore, eliminating excess ROS is a common function of fracture treatment materials. Dopamine can act as a signaling molecule in mediating this response, being reduced to dopamine quinone through redox reactions and involved in the regulation of oxidative stress.

We isolated BMDMs and cultured them on the scaffold, simulating the early microenvironment of a fracture by inducing an inflammatory response with lipopolysaccharide (LPS) (Fig. 4A). The stimulation with LPS resulted in decreased cell viability, but BMDMs cultured on the GAD/Ag-pIO scaffold showed significantly increased cell viability compared to the LPS group, demonstrating the anti-inflammatory effect of GAD/Ag-pIO (Fig. 4B). Next, we measured the levels of several inflammatory mediators. Enzyme linked immunosorbent assay (ELISA) results showed that LPS stimulation increased the levels of Tumor Necrosis Factor Alpha (TNF-α), IL-6 - Interleukin 6 (IL-6), and IL-1β - Interleukin 1 Beta (IL-1β) in BMDMs, while treatment with GAD/Ag-pIO effectively reduced the expression of pro-inflammatory cytokines, approaching the levels of the control group, whereas the GA group showed no significant effect (Fig. 4C-E).

During the early stages of fracture healing, high levels of ROS are one of the main causes of inflammation, and catechol groups can scavenge ROS and transform them into quinone groups [38]. The Ultraviolet (UV)-visible spectroscopy showed that the GAD/Ag-pIO scaffold displayed stronger 2,2-Diphenyl-1-picrylhydrazyl (DPPH) clearing ability compared to the GA scaffold, with further enhancement with the additional Ag-pIO, indicating that the major antioxidant effect is derived from Ag-pIO and possesses considerable ROS clearing ability (Fig. 4F). To

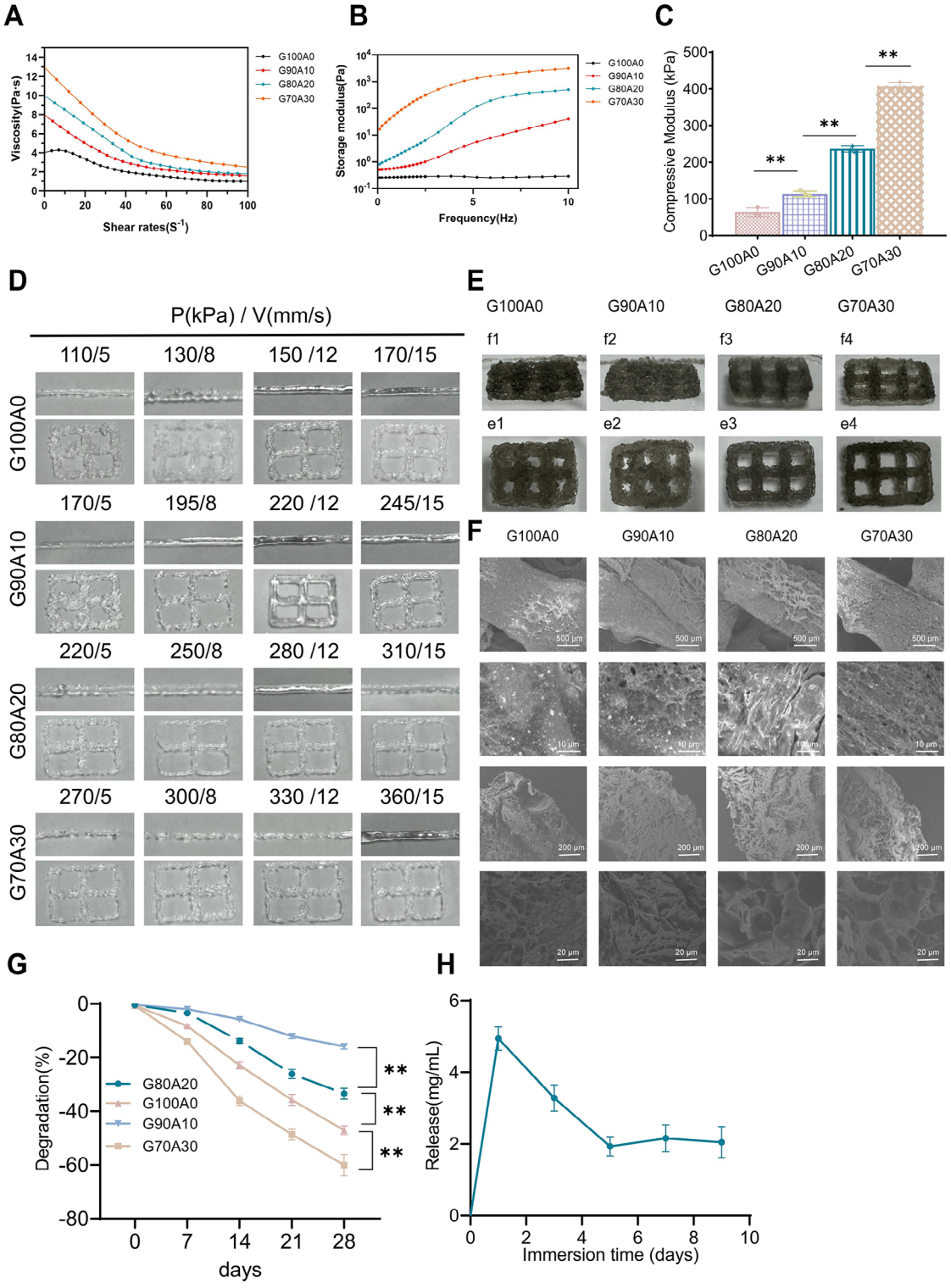

Fig. 3 Evaluation of the gel scaffold printed by 3D printing. *Note* (**A**) Detection of shear rate viscosity behavior; (**B**) Detection of shear storage modulus frequency; (**C**) Compression modulus measurement of different composition gels; (**D**) Optical photographs of printed gel under different printing parameter conditions; (**E**) Optical photographs of printed scaffold under optimal printing process conditions, top horizontal bar represents 700 μm, bottom horizontal bar represents 400 μm; (**F**) SEM images of the surface and cross-section of the printed scaffold, from top to bottom horizontal bar represents 500 μm, 10 μm, 200 μm, 20 μm; (**G**) Degradation rate measurement of 3D printed scaffold; (**H**) Silver ion release rate measurement of 3D printed scaffold. The experiment was repeated three times; ** indicates $P < 0.01$

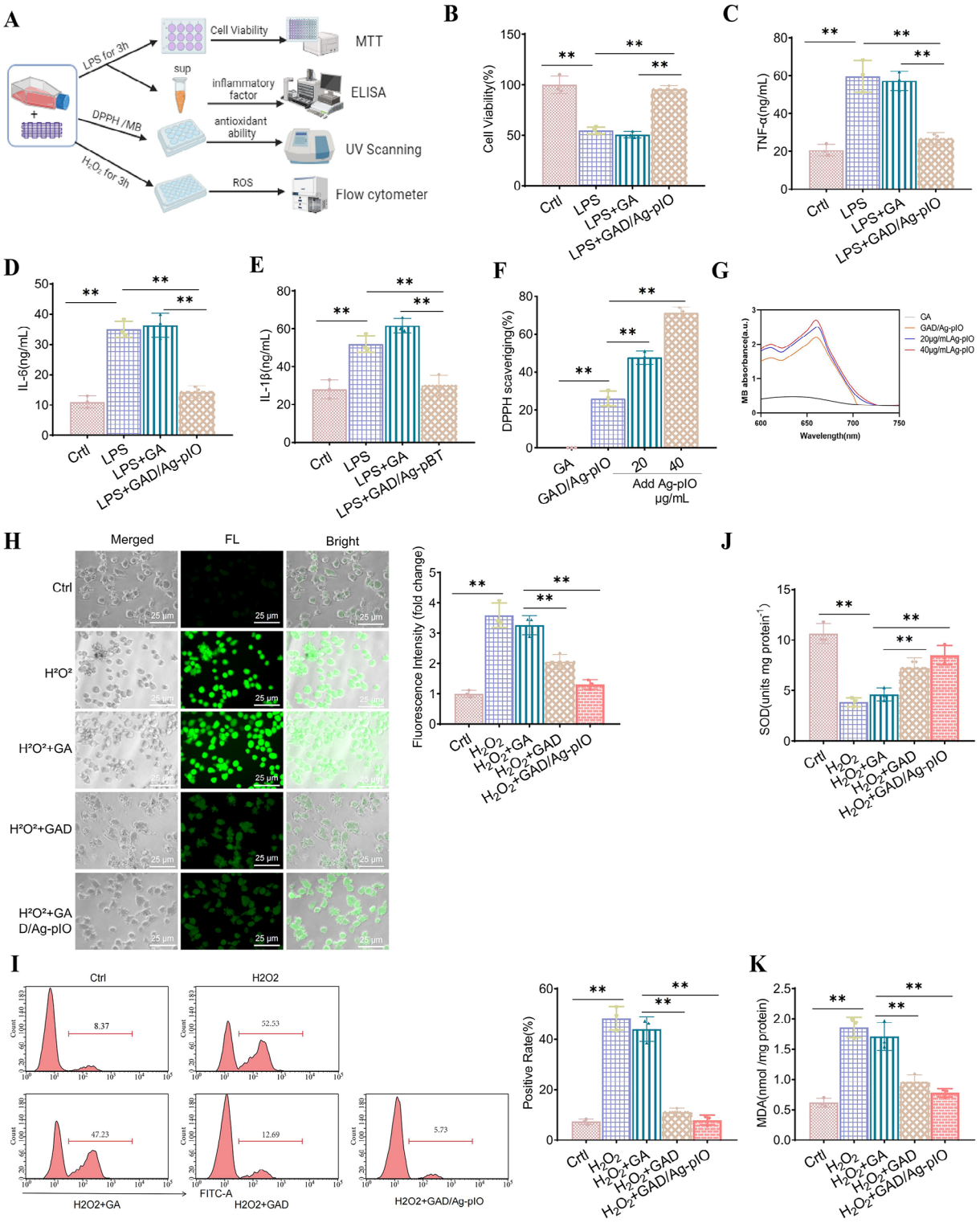

Fig. 4 Study on the immunomodulatory and antioxidant activity of the 3D printed gel scaffold. *Note* (**A**) Schematic diagram of the experimental method process; (**B**) Measurement of cell viability using the MTT method; (**C**-**D**) Detection of TNF-a (C) and IL-6 (**D**) levels using the ELISA method; (**E**) Detection of IL-1β levels using an ELISA kit; (**F**) Clearance efficiency of DPPH free radicals measured using UV-visible spectroscopy; (**G**) Efficiency of different treatment conditions on the catalysis of MB measured using UV-visible absorption technique; (**H**) Brightfield and fluorescence images of different treatment groups, ROS in DCFH-DA stained cells appear green, bar = 500 μm; (**I**) Flow cytometric analysis of cells labeled with 2′,7′-DCFH-DA in different groups in the FITC-A channel, bar graph shows the subgroups of stained ROS and their percentages; (**J**) Measurement of SOD levels in different groups; (**K**) Measurement of MDA levels in different groups. The experiment was repeated three times: ** indicates $P < 0.01$

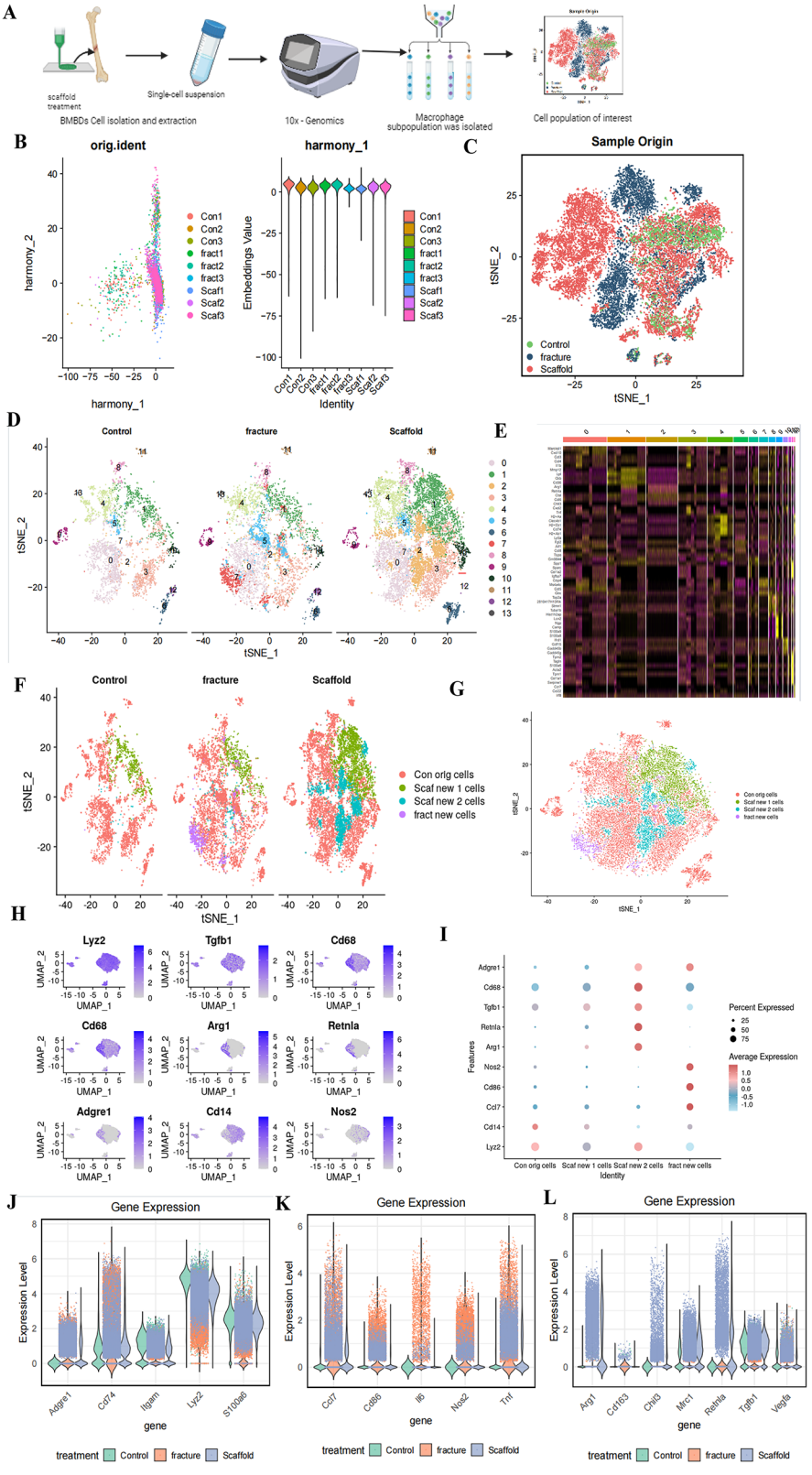

Fig. 5 (See legend on next page.)

(See figure on previous page.)

Fig. 5 Cell clustering of scRNA-seq data. *Note* (**A**) The schematic diagram of the in vitro culture technique for murine bone marrow macrophages near fracture; (**B**) After batch correction using Harmony, the distribution of cells in PC_1 and PC_2 was adjusted, where each point represents a single cell; (**C**) tSNE visualization of cell clustering, showing the aggregation and distribution of cells in normal, fracture, and scaffold treatment samples. Red represents scaffold treatment samples, blue represents fracture samples, and green represents normal samples; (**D**) tSNE visualization of cell clustering, displaying the aggregation and distribution of cells from different sources, with each color representing a cluster; (**E**) Heatmap of highly variable genes in each cluster, where yellow indicates significantly high expression; (**F**) Group visualization of cell annotation results based on tSNE clustering; (**G**) Visualization of cell annotation results based on tSNE clustering, where each color represents a cell subpopulation, and each subpopulation is highlighted with a different colored circle; (**H**) Expression levels of marker genes in different cell subpopulations, with darker shades of blue indicating higher average expression levels; (**I**) Bubble plot showing the expression levels of marker genes in different cell subpopulations, with darker shades of red indicating higher average expression levels; (**J**-**L**) Total expression levels of marker genes for M0 macrophage subpopulation, M1 macrophage subpopulation, and M2 macrophage subpopulation in different samples

understand its catalytic mechanism, we further reacted the scaffold with methylene blue (MB), which can eliminate ·OH radicals generated in the Fenton reaction [39]. Compared to the GA scaffold, the GAD/Ag-pIO scaffold exhibited stronger catalytic activity, which further increased with the addition of extra Ag-pIO (Fig. 4G).

To demonstrate the GAD/Ag-pIO scaffold's ability to eliminate cellular ROS, we utilized a DCFH-DA probe to investigate intracellular ROS levels. The blank group exhibited low ROS levels, while the H_2O_2 group showed increased oxidative stress. Interestingly, in the H_2O_2+GA group, ROS levels remained relatively unchanged, indicating the hydrogel matrix itself lacks ROS scavenging capabilities. However, in both the H_2O_2+GAD and H_2O_2+GAD/Ag-pIO groups, ROS levels significantly decreased, with the H2O2+GAD/Ag-pIO group approaching levels similar to the blank group, suggesting that GAD/Ag-pIO reinforces cellular protection against oxidative stress (Fig. 4H). Flow cytometry results revealed that the ROS-positive rate induced by H2O2 was 34.07%, reduced to 10.84% in the H_2O_2+GAD group, and further decreased to 6.84% in the H_2O_2+GAD/Ag-pIO group (Fig. 4I). Furthermore, the GAD/Ag-pIO scaffold enhanced the expression of cellular antioxidant enzymes, directly clearing ROS, thus safeguarding cells from oxidative stress-induced damage (Fig. 4J). The GAD/Ag-pIO scaffold notably decreased the levels of malondialdehyde (MDA) induced by hydrogen peroxide in cells to 0.707±0.050 nmol/mg protein, comparable to the MDA levels in normal cells (0.663±0.051 nmol/mg protein), effectively alleviating cellular oxidative stress (Fig. 4K).

In conclusion, the GAD/Ag-pIO scaffold possesses bioactivity that enhances immunity, clears ROS, and inhibits oxidative stress, thereby having the potential to reduce oxidative damage at the site of fracture during the healing process.

Analysis of macrophage subcluster expression profile and its impact on scaffold treatment in fracture healing

Immune cells, particularly macrophages, play a crucial role in the process of fracture healing. Among the earliest immune cells to respond to fractures, macrophages remain actively involved throughout the healing process. Studies have shown that macrophages have the ability to regulate the differentiation and function of osteoblasts [40, 41]. Specifically, different phenotypes of macrophages, such as the classically activated (M1) and alternatively activated (M2) macrophages, have distinct roles in the healing process. Delayed or failed fracture healing has been associated with overexpression of pro-inflammatory cytokine-secreting M1 macrophages and downregulation or ineffectiveness of the anti-inflammatory response mediated by M2 macrophages. Consequently, promoting M2 macrophage polarization and/or inhibiting M1 macrophage differentiation may contribute to the healing of fractures.

To investigate this, we isolated macrophages from the bone marrow of normal control group mice, bone marrow adjacent to the fracture site of mice at 72 h after fracture, and bone marrow adjacent to the fracture site of mice treated with 3D printed GAD/Ag-pIO scaffold for 72 h. These samples were labeled as the Control group, fracture group, and Scaffold group, respectively. Subsequently, we performed in vitro culture of these macrophages. Single-cell RNA extraction and library construction were conducted using the Illumina NovaSeq 6000 system, generating a large amount of transcriptional data (Fig. 5A). The results revealed that the majority of cells had nFeature_RNA<5000, nCount_RNA<20,000, and percent.mt<20% (Fig. S6A). To improve data quality, we excluded low-quality cells based on the criteria of 200<nFeature_RNA<5000 and percent.mt<25%, resulting in an expression matrix of 16,961 genes and 21,367 cells. In the filtered data, the correlation coefficient between nCount_RNA and percent. mt is r = -0.16, while the correlation coefficient between nCount_RNA and nFeature_RNA is r=0.9 (Fig. S6B), indicating the satisfactory quality of the filtered cell data for further analysis.

To analyze the filtered cells further, we selected the top 2000 genes with the highest gene expression variance for downstream analysis (Fig. 5B). The CellCycleScoring function was used to calculate the cell cycle of the sample cells (Fig. S6C), followed by normalization of the data. Principal component analysis (PCA) was then employed to perform linear dimensionality reduction on the data.

A heatmap of the expression of the top correlated genes for PC_1 to PC_6 was displayed (Fig. S6D), along with the distribution of cells in PC_1 and PC_2 (Fig. S6E). The results demonstrated no significant batch effects between the samples.

To further reduce batch effects and improve the accuracy of cell clustering, we employed the Harmony software package to perform batch correction on the sample data (Fig. S6F-H). The corrected results showed effective elimination of batch effects (Fig. 5C). Additionally, an ElbowPlot was used to rank the standard deviation of the principal components, revealing that PC_1 to PC_20 adequately reflected the information contained within the highly variable genes and were of significant analytical significance (Fig. 5D).

Next, we applied the t-SNE algorithm to perform nonlinear dimensionality reduction on the top 20 principal components. Through clustering, we obtained 14 clusters (Fig. 5E), and a heatmap displaying the top 5 highly variable genes for each cluster was presented. By studying the distribution of different clusters in different samples, we observed the appearance of a new cluster 7 in the fracture samples compared to the normal samples and the appearance of two new clusters 1 and 2 in the scaffold-treated samples compared to both the normal and fracture samples. Therefore, we defined the clusters 0, 3, 4, 5, 6, 8, 9, 10, 11, 12, and 13, which were present in all three samples, as "Con Orig cells" (clusters of normal sample original cells); we defined cluster 7 as "fact new cells" (cluster of fracture cells); and we defined clusters 1 and 2 as "Scaf new 1 cells" and "Scaf new 2 cells" (clusters of scaffold-treated cells 1 and 2) respectively. Subsequently, cell annotations were performed, resulting in the identification of 4 cell subclusters (Fig. 5F-G). Based on the literature search for known cell lineage-specific marker genes, combined with using the online database CellMarker for identifying mouse macrophage marker genes, we presented the Uniform Manifold Approximation and Projection (UMAP) expression plots (Fig. 5H) and bubble plots (Fig. 5I) showcasing the marker genes of different subclusters. The expression profiles of the marker genes indicated that the newly emerged subclusters exhibited more distinct characteristics of M1 and M2 macrophages. We calculated the total expression levels of marker genes for the M0 macrophage subcluster (Fig. 5J), M1 macrophage subcluster (Fig. 5K), and M2 macrophage subcluster (Fig. 5L) in different samples. The results indicated a significant increase in the expression of M1 macrophage marker genes in the fracture samples and a significant increase in the expression of M2 macrophage marker genes in the scaffold-treated samples.

Our single-cell analysis results were validated through in vivo immunofluorescence experiments. On the 7th day of fracture healing, immunofluorescence imaging displayed a significant increase in the expression of TNF-α and iNOS-positive M1 macrophages in the fracture model group, while the Model+GAD/Ag-pIO treatment group exhibited a significant increase in the expression of CD163-positive M2 macrophages (Fig. S7).

To summarize, our findings suggest the emergence of new subclusters in macrophages following fracture and further changes in macrophage subclusters after scaffold treatment. In the fracture samples, there were more M1 macrophages, while the scaffold-treated samples exhibited a greater presence of M2 macrophages.

Protection of macrophage mitochondria from ROS damage and promotion of mitochondrial transfer by GAD/Ag-pIO, enhancing bmscs proliferation and osteogenic differentiation

Previous experiments have demonstrated that GAD/Ag-pIO possesses the ability to function as an antioxidant and eliminate ROS while also promoting M2 polarization of macrophages in the bone fracture microenvironment. To investigate whether GAD/Ag-pIO can protect macrophages from ROS damage, we included the ROS scavenger N-acetylcysteine (NAC) as a control. The results of TMRE staining indicate that GAD/Ag-pIO can preserve mitochondrial membrane potential and prevent mitochondrial fragmentation from damage under oxidative stress induced by LPS stimulation. The findings suggest that GAD/Ag-pIO possesses the ability to protect and maintain mitochondrial integrity (Fig. 6A-B).

During bone repair, macrophages accumulate in the damaged area and produce a variety of biologically active factors such as bone morphogenetic proteins (BMPs), vascular endothelial growth factor (VEGF), and transforming growth factor β (TGF-β). These factors can promote the differentiation of BMSCs into osteoblasts or key osteogenic factors, thereby facilitating the generation and repair of new bone tissue [42]. Recently, a novel mode of communication relying on intercellular organelle transfer has garnered significant attention [43]. Furthermore, intercellular mitochondrial transfer has been found to play a role in cellular metabolism, immune response, mitochondrial quality control, wound healing, tissue integrity, and other physiological regulations [44]. We hypothesized the existence of a novel mitochondrial communication pathway between macrophages and BMSCs that can impact cellular functions.

To test this hypothesis, we labeled mitochondria in macrophages with the MitoTracker probe, then re-cultured the macrophages in a fresh medium and exposed them to LPS as a conditioned medium. FACS analysis was performed to collect mitochondrial signals from the medium, and the results demonstrated that GAD/Ag-pIO and NAC were able to rescue the damaged mitochondrial signals in the medium (Fig. 6C). Additionally,

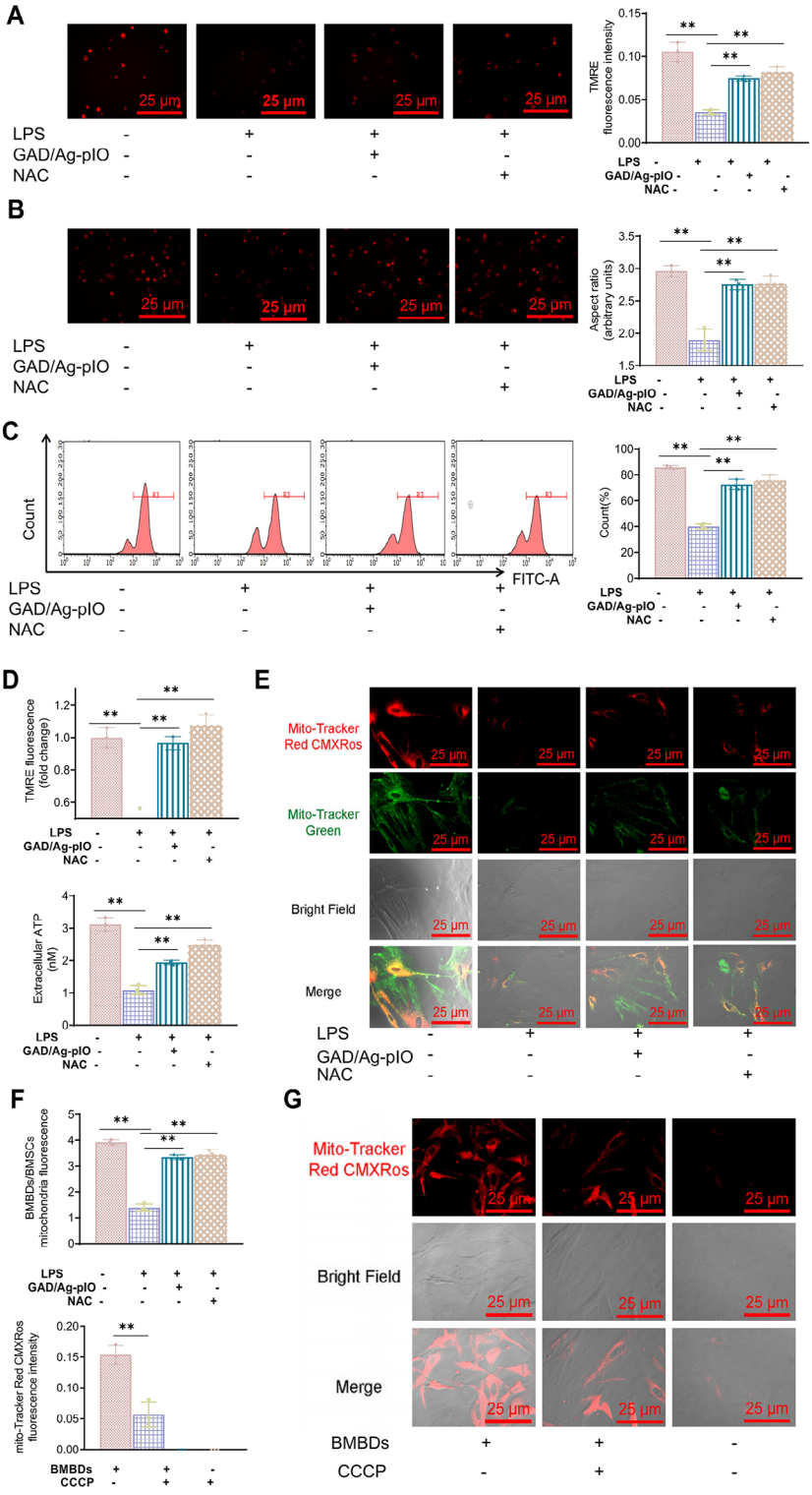

Fig. 6 GAD/Ag-pIO promotes mitochondrial transfer in macrophages. *Note* (**A**) Mitochondrial membrane potential in macrophages under different treatment conditions, bar = 50 μm; (**B**) Observation of mitochondrial structure in macrophages under different treatment conditions, upper bar = 10 μm, lower bar = 5 μm; (**C**-**D**) Mitochondrial signal and membrane potential in macrophage-conditioned medium; (**E**) ATP production in macrophage-conditioned medium; (**F**) Representative images and quantification of mitochondrial signal in BMSCs cultured in macrophage-conditioned medium after specified treatment, bar = 10 μm; (**G**) Representative images and quantification of mitochondrial signal in BMSCs cultured in macrophage-conditioned medium treated with CCCP, bar = 10 μm. Cell experiments were repeated three times, $^{**}p < 0.01$

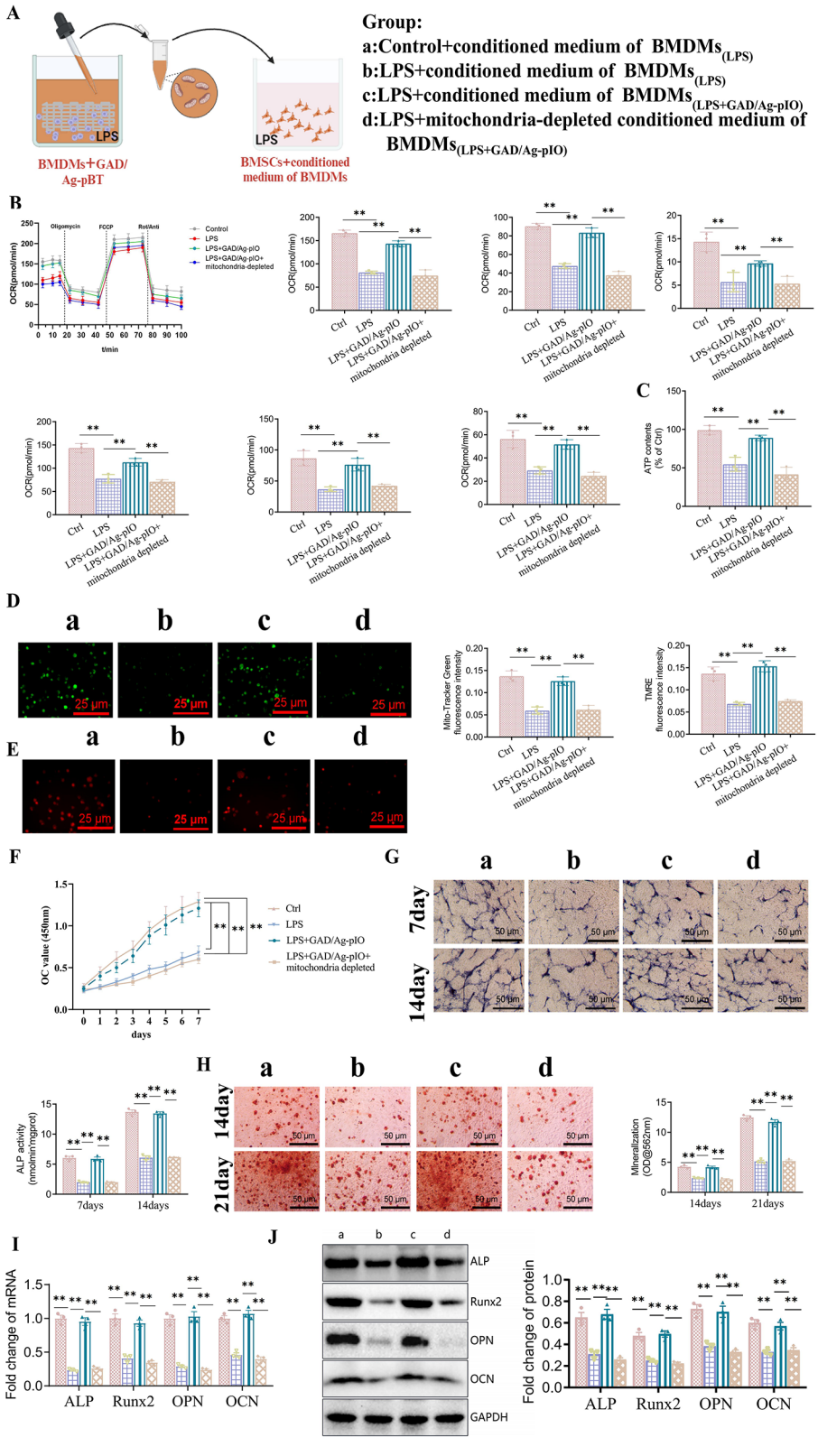

Fig. 7 (See legend on next page.)

(See figure on previous page.)

Fig. 7 Experimental validation of macrophage-mediated mitochondrial transfer promotes osteogenic differentiation of BMSCs. *Note* (**A**) Schematic diagram of different groups of BMSCs in treatment; (**B**) Measurement of oxygen consumption rate in BMSCs under different treatment conditions; (**C**) Cellular ATP levels in BMSCs under different treatment conditions; (**D**-**E**) Representative images and quantification of mitochondrial signal (**D**) and membrane potential (**E**) in BMSCs from different treatment groups, scale bar = 50 μm; (**F**) Proliferation of BMSCs in different treatment groups; (**G**) ALP staining and statistical analysis of early osteogenic differentiation in BMSCs from different treatment groups, scale bar = 100 μm; (**H**) ARS staining and statistical analysis of late osteogenic differentiation in BMSCs from different treatment groups, scale bar = 100 μm; (**I**) Expression levels of osteogenic-related mRNA, including ALP, Runx2, OPN, and OCN, in BMSCs after 14 days of treatment in different groups; (**J**) Quantification of western blot analysis for expression of osteogenic proteins ALP, Runx2, OPN, and OCNDE in BMSCs from different treatment groups after 14 days. Cell experiments were repeated three times, denoting **denoting $P < 0.01$

GAD/Ag-pIO treatment also restored the mitochondrial membrane potential and ATP content in the collected medium (Fig. 6D-E), showing similar effectiveness as the NAC treatment group. These findings suggest that GAD/Ag-pIO can protect macrophage mitochondria from damage, thus ensuring mitochondrial quality.

To observe the mitochondrial transfer from macrophages to BMSCs, we isolated BMSCs and conducted adipogenic and osteogenic differentiation, chondrogenic differentiation, as well as surface marker identification (Fig. S8).

Subsequently, we cultured BMSCs in a conditioned macrophage-treated medium and observed the mitochondrial signals of both endogenous (BMSCs labeled with MitoTracker Green) and exogenous (macrophages labeled with Tracker Red CMXRos) origin. We found that culturing in medium from macrophages treated with LPS led to an approximately 3.0-fold decrease in mitochondrial signals between macrophages and BMSCs (Fig. 6F). However, GAD/Ag-pIO protected macrophages from damage and effectively restored mitochondrial signals in BMSCs when co-cultured in the conditioned medium (Fig. 6F). Treatment with carbonyl cyanide m-chlorophenyl hydrazone (CCCP), a substance that disrupts cellular energy metabolism and impacts mitochondrial function, resulted in a significant reduction of macrophage mitochondria in BMSCs (Fig. 6G), suggesting the maintenance of functional integrity during mitochondrial transfer from macrophages to BMSCs. Comparable results were observed with the ROS scavenger NAC when compared to the GAD/Ag-pIO treatment group.

Mitochondria play a crucial role in stem cells, including energy supply, regulation of non-oxidative metabolism, and ROS balance [45–47]. The transfer of macrophage mitochondria to BMSCs may influence stem cell metabolism, immune modulation abilities, cell proliferation, differentiation, and inflammatory regulation [48, 49].

To induce injury in BMSCs, we first exposed them to LPS and then cultured them in a conditioned medium derived from macrophages for 18 h. Details of the treatment conditions and nomenclature can be found in Fig. 7A. Co-culturing with a conditioned medium pretreated with GAD/Ag-pIO improved the metabolic capacity and adenosine triphosphate (ATP) production of BMSCs (Fig. 7B-C). However, this improvement disappeared when mitochondria were removed using a 0.2 μm filter, indicating that mitochondria transferred from macrophages have a protective effect on BMSCs. LPS caused inflammation and oxidative stress damage to BMSC mitochondria, resulting in decreased Oxygen Consumption Rate (OCR) levels. Nevertheless, incubation with a conditioned medium prepared from macrophages pre-treated with GAD/Ag-pIO was able to reverse these damages, while the medium without mitochondria failed to do so (Fig. 7B). Incubation with a conditioned medium prepared from GAD/Ag-pIO pre-treated macrophages increased macrophage mitochondrial signaling and membrane potential within BMSCs (Fig. 7D-E). These results suggest that promoting mitochondrial translocation in macrophages is one way GAD/Ag-pIO facilitates the recovery of BMSCs from oxidative stress damage.

To investigate the impact of macrophage mitochondria on BMSC proliferation and differentiation further, we added conditioned medium from macrophages to BMSC cultures. Methyl thiazolyl tetrazolium (MTT) assays showed that compared to the LPS-induced injury group, incubation with a conditioned medium prepared from macrophages pre-treated with GAD/Ag-pIO effectively restored BMSC proliferation after injury (Fig. 7F). ALP staining, an early marker of osteogenic differentiation, was significantly lower in the mitochondrial-depletion group and LPS-induced injury group compared to the group co-cultured with conditioned medium prepared from GAD/Ag-pIO pre-treated macrophages (Fig. 7G). ARS staining, assessing calcium mineral deposition as an important indicator of late-stage osteogenic differentiation, showed the highest number of mineralized nodules and enhanced positive staining in the group co-cultured with conditioned medium prepared from GAD/Ag-pIO pre-treated macrophages (Fig. 7H), indicating better osteogenic potential.

OPN and OCN are crucial components of bone ECM, while Runt-Related Transcription Factor 2 (Runx2) serves as a key transcription factor regulating osteogenic gene expression. Analysis at both mRNA and protein levels revealed a significant increase in the expression levels of ALP, Runx2, OPN, and OCN in the conditioned medium incubation group prepared from macrophages pretreated with GAD/Ag-pIO, compared to the LPS-induced

damage group (Fig. 7I-J), aligning with the ALP and ARS assessment results.

In conclusion, these data suggest that GAD/Ag-pIO, through its anti-oxidative stress effects, ensures the effective transfer of mitochondria from macrophages, whereby the transfer of macrophage mitochondria to BMSCs can restore oxidative stress damage, promote BMSC proliferation and osteogenic differentiation, upregulate the gene expression of ALP, Runx2, OPN, and OCN, thus facilitating bone healing.

GAD/Ag-pIO hydrogel synergizes with mitochondria to promote bone fracture healing in mice

We have successfully established a standardized mouse fracture model for mouse fracture therapy, utilizing 3D-printed GA scaffolds and GAD/Ag-pIO scaffolds to observe the therapeutic efficacy of GAD/Ag-pIO scaffolds on the fracture healing process. The specific experimental procedure involved culturing macrophages on GAD/Ag-pIO scaffolds for 5 days, extracting the cultured macrophage mitochondria (mito), loading them into GAD/Ag-pIO hydrogel, and preparing GAD/Ag-pIO+mito scaffolds for fracture treatment. Details of the experimental groups and evaluation criteria are provided in Fig. 8A. We have successfully established a standardized mouse fracture model for mouse fracture therapy, utilizing 3D-printed GA scaffolds and GAD/Ag-pIO scaffolds to observe the therapeutic effects of the GAD/Ag-pIO scaffold on the fracture healing process. The specific experimental procedure involved culturing macrophages on GAD/Ag-pIO scaffolds for 5 days, extracting the cultured macrophage mitochondria (mito), loading them into GAD/Ag-pIO hydrogel, and preparing GAD/Ag-pIO+mito scaffolds for fracture treatment. Details of the experimental groups and evaluation criteria are provided in Fig. 8A.

First, in order to better understand the effects of GAD/Ag-pIO on inflammatory responses and macrophage activation during the fracture healing and regeneration process, we utilized immunohistochemical staining for superoxide dismutase 1 (SOD1) and IL-1β, as well as immunofluorescent staining for CD86 as a surface marker for M1 and CD206 as a surface marker for M2 macrophages, to evaluate their in vivo antioxidative and immunomodulatory properties. At all three time points, the SOD1 levels in the Normal group were consistently lower. In comparison to the Normal group, the Model group showed a significant increase in SOD1 levels. The SOD1 levels in the GA group did not significantly differ from the Model group, indicating that the gelatin matrix itself has no harm or immunomodulatory effect on fractures. The SOD1 levels in the GAD/Ag-pIO and GAD/Ag-pIO+mito groups were both lower than those of the Model group, consistent with the results of the in vitro antioxidative ROS clearance ability. The M2 macrophage mitochondrial SOD1 levels in the GAD/Ag-pIO+mito group were slightly higher than the GAD/Ag-pIO group (Fig. 8B). The IL-1β levels in the Normal group were consistently lower. In comparison to the Normal group, the Model group showed a significant increase in IL-1β levels. The IL-1β levels in the GA group did not significantly differ from the Model group, suggesting that the gelatin matrix itself has no harm or immunomodulatory effect on fractures. The expression levels of the inflammatory mediator IL-1β in the GAD/Ag-pIO and GAD/Ag-pIO+mito groups were significantly lower than the GA group at all three time points, with the GAD/Ag-pIO+mito group being significantly higher than the GAD/Ag-pIO group at day 3 and day 7, indicating that macrophage-derived mitochondria can improve the inflammatory environment of fractures (Fig. 8C). The typical CD86 (green) and CD206 (red) immunofluorescent co-localization images used for the fracture treatment and corresponding quantitative results revealed that at day 3, the macrophages in the Model, GA, and GAD/Ag-pIO groups were predominantly in a pro-inflammatory state (M1 phenotype). The number of CD86-positive cells in the GAD/Ag-pIO group was significantly lower than the GA group, and the GAD/Ag-pIO+mito group was significantly lower than the GAD/Ag-pIO group. Mild immune reactions play a crucial role in recruiting BMSCs for osteogenesis, and as time progresses, the immune reaction gradually weakens, with the GAD/Ag-pIO and GAD/Ag-pIO+mito groups showing a significantly faster rate of decline than the GA group (Fig. 8D). At day 7, the number of CD206-positive cells in the GAD/Ag-pIO and GAD/Ag-pIO+mito groups significantly increased, indicating an anti-inflammatory M2 phenotype, with the GAD/Ag-pIO+mito group having a significantly higher number of CD206-positive cells than the GAD/Ag-pIO group. At day 14, the GAD/Ag-pIO and GAD/Ag-pIO+mito groups entered the inflammatory regulatory balance state earlier than the GA group, with a predominant anti-inflammatory M2 phenotype and no significant difference between the GAD/Ag-pIO and GAD/Ag-pIO+mito groups. These in vivo experimental results demonstrate the good immunomodulatory properties of GAD/Ag-pIO and the ability of macrophage-derived mitochondria to promote the inflammatory regulation of the fracture microenvironment to reach a balanced state more quickly.

To dynamically observe the healing process of fractures, we conducted observations of the fracture site on postoperative days 7 and 35. Hematoxylin and eosin staining revealed that on postoperative day 7, there were similar patterns of granulation tissue growth in all groups, with minimal observed differences. As the treatment duration extended, the granulation tissue gradually

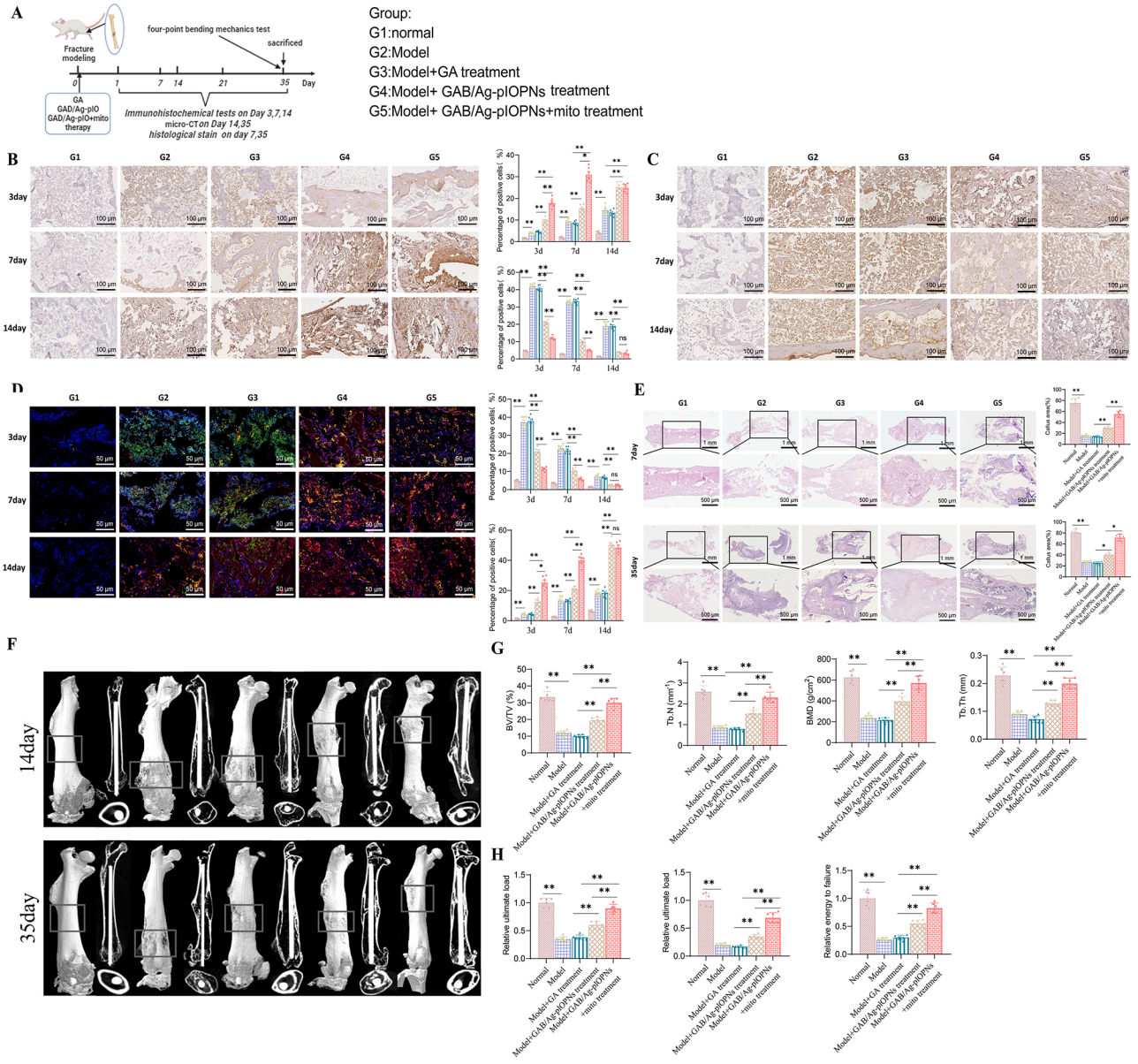

Fig. 8 Effects of different implanted stents on the healing process of mouse fractures. *Note* (**A**) Schematic diagram of different time points for in vivo experimental indicators and annotations for groups G1-G5 in Fig. 8B-H; (**B**) Immunohistochemical staining images and statistical graphs of SOD1, bar = 100 μm; (**C**) Immunohistochemical staining images and statistical graphs of interleukin-1β (IL-1β), bar = 100 μm; (**D**) Immunofluorescence co-localization images and statistical graphs of CD86 (M1) and CD206 (M2), bar = 50 μm; (**E**) H&E staining images and statistical graphs of femurs collected from mice on day 7 and day 35 after surgery, bar = 500 μm; (**F**) micro-CT images of femurs collected from mice on day 14 and day 35 after surgery. White boxes indicate the ROI for microCT analysis, bar = 10 mm; (**G**) MicroCT parameter evaluation (BV/TV, Tb.N, BMD, Tb.Th); (**H**) Biomechanical testing of fracture healing. Each group consisted of 6 mice. ** indicates $P < 0.01$ when compared between two groups, and "ns" indicates no significant difference when compared between two groups

formed. On postoperative day 35, the morphology of the callus in the GAD/Ag-pIO group and the GAD/Ag-pIO+mito group had transformed into an oval shape, completely surrounding the fracture ends. Particularly in the GAD/Ag-pIO+mito group, newly formed cortical bone was observed within the granulation tissue. Additionally, the distribution of trabeculae within the granulation tissue was dense, uniform, and well-organized in both of these groups, indicating that the growth of granulation tissue was accelerated and the fracture repair was more complete (Fig. 8E).

The 3D reconstructions of MicroCT on postoperative day 14 showed that there were minimal callus formations and larger gaps at the fracture site in both the Model group and the GA group. Comparatively, there were more callus formations and smaller gaps in the

GAD/Ag-pIO group and the GAD/Ag-pIO+mito group, with a larger newly formed callus area in the GAD/Ag-pIO+mito group than in the GAD/Ag-pIO group. On postoperative day 35, incomplete healing gaps were observed in the Model group and the GA group, while minimal gaps and more callus tissue were observed in the GAD/Ag-pIO group and the GAD/Ag-pIO+mito group (Fig. 8F). Compared to the GA group, the GAD/Ag-pIO and GAD/Ag-pIO+mito treatment groups exhibited a significant increase in bone volume/total volume (BV/TV) and trabecular thickness (Tb.Th) at the fracture site, with the GAD/Ag-pIO+mito treatment group having more pronounced effects (Fig. 8G).

Further biomechanical analysis indicated that the GAD/Ag-pIO group and GAD/Ag-pIO+mito group promoted fracture healing, with the GAD/Ag-pIO+mito group exhibiting more significant effects due to the greater secretion of growth factors and mitochondrial substances providing a material basis for osteogenesis-related processes (Fig. 8H).

These results demonstrate that GAD/Ag-pIO hydrogel has a promotive effect on fracture healing in the mouse fracture model, and the addition of conditionally treated macrophage mitochondria further enhances the fracture healing process.

Discussion

The healing of bone fractures is crucial for the restoration of skeletal function, and the osteogenic differentiation of BMSCs plays a key role in this process [50, 51]. Macrophages are a type of immune cell, and recent studies have found that macrophages may influence the osteogenic differentiation of stem cells by regulating mitochondrial function [52–54]. Previous studies have primarily focused on investigating the impact of factors such as cytokines and signaling pathways on the osteogenic differentiation of BMSCs while overlooking the role of macrophage mitochondrial function in this process [55, 56]. Therefore, this study offers a novel perspective by exploring how immunomodulatory 3D hydrogel scaffolds regulate macrophage mitochondrial transfer to enhance the osteogenic differentiation of BMSCs, thereby advancing research on the mechanisms underlying bone fracture healing.

Macrophages play a significant role in immune regulation and bone fracture healing [57–59]. Previous studies have shown that macrophages can differentiate into two subtypes, M1 and M2, which have different functions [60–62]. This study demonstrates that treatment with the GAD/Ag-pIO scaffold can significantly alter the distribution of macrophage subtypes, promoting M2 polarization in macrophages. At the same time, it was discovered that mitochondrial transfer in macrophages also positively influences the osteogenic differentiation of BMSCs. These results indicate that macrophage function and mitochondrial transfer both play important regulatory roles in the process of bone fracture healing.

In this study, an in-situ growth method was used to prepare a 3D biomimetic hydrogel scaffold with immunomodulatory properties (GAD/Ag-pIO) [63–65]. Cell experiments demonstrated that the scaffold exhibited good biocompatibility and possessed immune-modulating properties. Through in vitro fluorescence tracking observations, it was found that under the treatment of the GAD/Ag-pIO scaffold, macrophage mitochondria could successfully transfer into BMSCs and promote their osteogenic differentiation. Furthermore, animal experiments further confirmed the promoting effect of the GAD/Ag-pIO scaffold on bone fracture healing.

In conclusion, this study extensively investigates the application of the GAD/Ag-pIO 3D biocompatible hydrogel scaffold in promoting the osteogenic differentiation of BMSCs and fracture healing (Fig. 9). The developed GAD/Ag-pIO 3D biocompatible hydrogel scaffold combines the characteristics of biocompatibility, immune modulation, and promotion of BMSCs' osteogenic differentiation. This material's design not only brings innovation to the field of material science but also provides new insights for fracture treatment and tissue engineering. The study not only demonstrates the scaffold's ability to promote the osteogenic differentiation of BMSCs but also reveals the mechanism of macrophage involvement in this process, which is of significant importance for a deeper understanding of the biological basis of BMSCs in bone repair and regeneration. The study finds that macrophages regulated by the GAD/Ag-pIO scaffold significantly influence the osteogenic differentiation of BMSCs, providing a new understanding of the interaction between immune cells and stem cells and serving as a basis for the development of immune modulation-based tissue engineering strategies. In vivo and in vitro experiments confirm the scaffold's promotion of BMSCs' osteogenic differentiation and its potential application in fracture treatment, which is of great significance in accelerating fracture healing and reducing patient suffering and recovery time.

However, this study still has some limitations. Firstly, although the promotion effect of the GAD/Ag-pIO scaffold on fracture healing was observed through in vivo animal experiments, more clinical trials are needed to validate its safety and efficacy further. Secondly, this study's research subjects were limited to mice, and further research is required to confirm if similar effects can be achieved in humans. Additionally, the specific mechanism of macrophage mitochondria transfer in this study remains unclear, and further in-depth research is needed to decipher the molecular mechanisms involved.

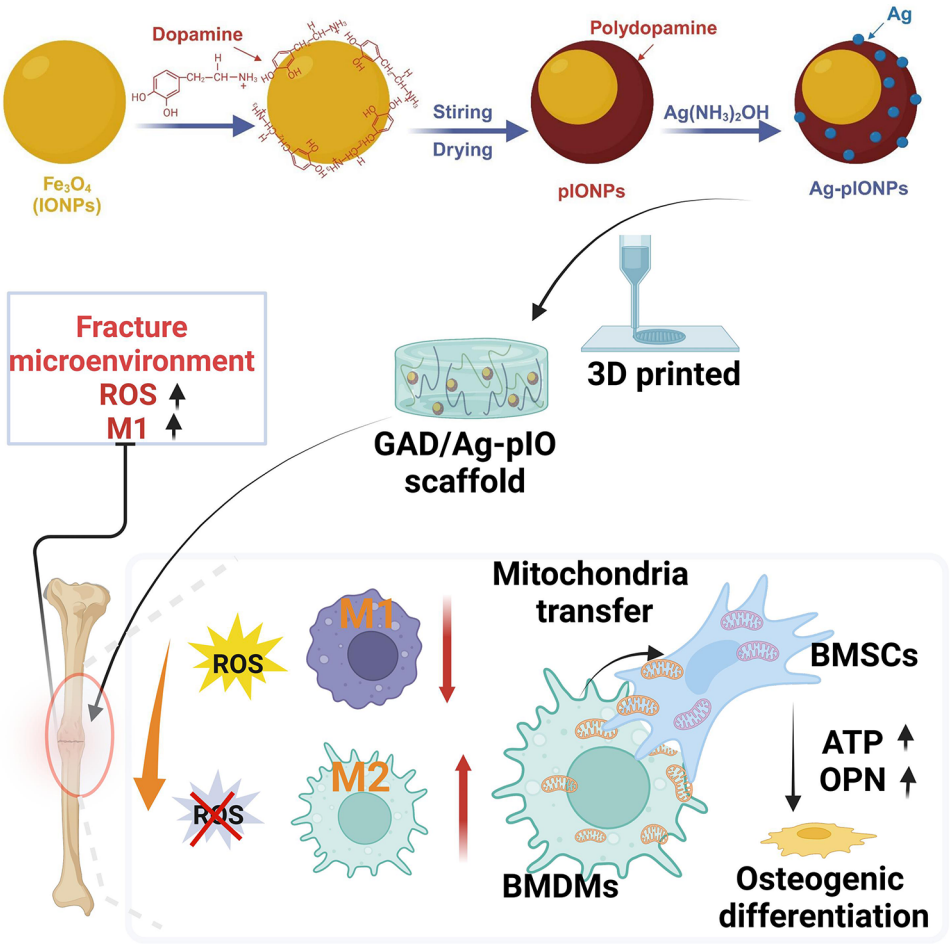

Fig. 9 Mechanism diagram of 3D printed GAD/Ag-pIO scaffolds for fracture treatment

Looking ahead, further research can focus on optimizing the preparation methods of the 3D biocompatible hydrogel scaffold to improve its biocompatibility and therapeutic effects. Moreover, studying the subgroups of macrophages and their different functions in the fracture healing process can better regulate macrophage activity and promote the healing process. Furthermore, exploring other immune modulation methods and strategies can further enhance the efficacy of fracture treatment. These further studies will contribute to further refining and expanding the application value of this research, providing more effective and innovative methods and approaches for fracture treatment.

Materials and methods

Preparation of Ag-pIOPNs nanoparticles

To prepare Ag-pIOPNs nanoparticles, 3 g of IOPNs powder (XFJ119-12227-89-3102138, Nanjing Xianfeng Nanomaterials Technology Co., Ltd.) was dispersed in a dopamine solution (2 g/L) (dopamine hydrochloride (DA-HCl, 99%, BP468, CAS: 62-31-7, Aladdin) at 60 °C for 12 h. The suspension was then centrifuged and washed with deionized water to remove residual dopamine. After drying, the resulting polydopamine-modified IOPNs were labeled as pIOPNs. Subsequently, a silver ammonia solution (0.06 mol/L) was prepared by dropping an ammonia solution ($NH_3{\cdot}H_2O$, 105423, CAS: 1336-21-6, Sigma-Aldrich) into a silver nitrate solution (0.17 mol L^{-1}, $AgNO_3$, 209139, Sigma-Aldrich). Next, 0.7 g of pIOPNs powder was added to the prepared silver ammonia solution (40 mL) and stirred continuously for 2 h. Finally, Ag-modified pIOPN nanoparticles were obtained by centrifugation, washing, and drying.

Analysis and characterization of materials

The morphology and elemental distribution of the samples were examined using a scanning electron microscope (SEM, S-4800, Hitachi, purchased from Shanghai Fulai Optical Technology Co., Ltd.), TEM (Hitachi H-7650, purchased from Shanghai Baihe Instrument Technology Co., Ltd.), and energy dispersive spectrometer (EDS, Bruker QUANTAX EDS). The powder morphology was observed using a TEM (FEI, USA). The chemical structure of the samples was analyzed using Fourier-transform

infrared spectroscopy (FT-IR, 912A0770, Thermo Fisher, USA). The size distribution of the nanoparticles and the zeta potential were measured using a nanoparticle tracking analyzer (Zeta View_Particle Metrix, purchased from Dachang Huajia Scientific Instruments) (all sample solutions were measured at pH 7.0) [66, 67]. The thermal stability of the samples was determined using a thermogravimetric analyzer (TGA-601, Nanjing Huicheng Instruments and Meters Co., Ltd.) under a nitrogen atmosphere at a heating rate of 20 °C/min. The compressive performance of the composite material scaffold was tested using a universal mechanical testing machine (CMTS5205, MTS, USA) at a constant deformation rate of 2.5 mm/min until the specimen height decreased by 40%. The compressive modulus was calculated from the slope of the initial linear region of the stress-strain curve. The release of ions from the scaffold in deionized water was quantitatively analyzed using an inductively coupled plasma optical emission spectrometer (ICP-OES, Spectro Blue Sop, purchased from Germany Hua Pu General Distribution).

3D printing and printability testing of hydrogels

Hydrogels were printed using the extrusion-based 3D printer (AXO A3) from Axolotl BIOSYSTEMS. Prior to printing, the hydrogel precursor was loaded into a 22 g syringe and injected into a 5 ml syringe. Printing parameters were set as follows: both the syringe and nozzle temperature were set to 31 °C, while the printing speed and pressure were adjusted accordingly. The hydrogel was sequentially printed onto a platform maintained at 4 °C, forming 1, 2, 5, and 10 layers. Subsequently, the printed hydrogel was immersed in a 1% calcium chloride solution for 2 min to allow for curing. Morphological observations were made on the cured hydrogel. Optimal process parameters were selected for the preparation of 3D-printed scaffolds.

Preparation of hybrid gel

Collagen (EFL-GEL-001, Suzhou Intelligent Manufacturing Research Institute), sodium alginate (EFL-Alg-300 K, Suzhou Intelligent Manufacturing Research Institute), or dopamine-modified sodium alginate (C6H7O6Na, molecular weight: 216.12) along with self-prepared Ag-pIOPNs were dissolved and dispersed. A solution of 0.25% (w/v) collagen and 0.1% (w/v) sodium alginate in PBS (pH 7.4) was stirred in a water bath at 70 °C for 30 min to obtain pre-fabricated water gelatin with the acronym GA. Subsequently, the GA prefabricated water gel was immersed in a 100mM calcium chloride solution (C4901, Sigma-Aldrich) for 48 h to solidify and form GA hydrogel [68]. In accordance with a cited reference [69], dopamine-modified sodium alginate (Alg-DA) was formed under the catalysis of EDC (1-(3-dimethylaminopropyl)-3-ethylcarbodiimide hydrochloride) and NHS (N-hydroxysuccinimide), which was then mixed with the collagen solution to prepare GAD hydrogel. Ag-pIOPNs were sonicated in water using an ultrasonic cleaner (US-22D, China Scientific Instruments (Beijing) Co., Ltd.) to form an ion-crosslinked primary network, subsequently loaded into the GAD hydrogel to prepare GAD/Ag-pIO hydrogel [70].

Rheological analysis

Rheological measurements were conducted using an Anton Paar MCT 302 rheometer (Anton Paar, Austria) at 37 °C. To evaluate shear-thinning behavior, the bioink was placed between parallel plates and subjected to increasing shear rates (0.01 to 200 s^{-1}). To assess the viscosity of the bioink prior to printing, the bioink underwent low shear at 1 s^{-1} for 600 s. Subsequently, the bioink was solidified into gel sheets with a diameter of 10 mm and a height of 1 mm. Scans were performed under fixed strain and frequency conditions (1% strain and 5 rad s^{-1}) for 300 s to evaluate the storage modulus and loss modulus [71]. Each experiment was conducted in triplicate.

Swelling ratio and degradation rate

Circular disc-shaped samples with a diameter of 8 mm and a height of 3 mm were prepared using bioink solutions of varying concentrations to calculate the swelling ratio. The samples were immersed in PBS at 37 °C for 12 h and weighed as M1, then lyophilized for 12 h and weighed as M2. The swelling ratio (Qs) was calculated using the equation Qs=M1/M2. Degradation experiments were conducted by placing the samples in a 24-well plate containing collagenase I (1148089, Merck, Germany) at a concentration of 0.5 mg/mL. The samples were removed at different time points, lyophilized, and weighed as mass (Wr). The initial sample mass was denoted as W0, and the degradation rate (Qd) was calculated as Qd=Wr/W0 [72]. Each experiment was performed in triplicate.

Isolation, cultivation, and identification of primary cells

BMSCs were collected from the tibia and femur of 7–8 week-old C57BL/6 mice (213, Beijing Vital River Laboratory Animal Technology Co., Ltd.) weighing 16–20 g. The bone marrow was washed with Dulbecco's Modified Eagle Medium (DMEM)/F12 (DF-041, Sigma Aldrich, Shanghai, China) to obtain a mixed cell suspension. The suspension was centrifuged at 800 g for 5 min to obtain a pellet containing BMSCs, which was resuspended in DMEM/F12 and cultured at 37 °C with 5% CO_2 [73]. The culture medium was replaced every 2–3 days.

Differentiation of BMSCs into adipocytes was induced using adipogenic induction medium (IMDM supplemented with 10% fetal bovine serum (FBS) (12103 C,

Sigma Aldrich, Shanghai, China), 10 μg/mL insulin (Y0001717, Sigma Aldrich, Shanghai, China), 1 μM dexamethasone (D1756, Sigma Aldrich, Shanghai, China), 0.5 mM phosphodiesterase (PDE) inhibitor (IBMX) (I5879, Sigma Aldrich, Shanghai, China), and 0.1 mM indomethacin (I7378, Sigma Aldrich, Shanghai, China)). Osteogenic differentiation of BMSCs was induced using osteogenic induction medium (IMDM supplemented with 10% FBS, 5 μg/mL insulin, 0.1 μM dexamethasone, 0.2 mM vitamin C (PHR1008, Sigma Aldrich, Shanghai, China), and 10 mM β-glycerophosphate (G5422, Sigma Aldrich, Shanghai, China)). ARS staining was used to assess calcium deposition at week 3 as an indicator of osteogenic differentiation, while Oil Red O staining was used to evaluate lipid droplet formation as an indicator of adipogenic differentiation at week 3. Cell morphology and growth were observed using an inverted microscope. Cell passaging was performed every 3–5 days when the cell confluence reached 80% [73–75].

Bone marrow-derived macrophages (BMDMs): Bone marrow progenitor cells were collected from the femur and tibia of 7–8 week-old C57BL/6 mice weighing 16–20 g. The progenitor cells were differentiated in RPMI-1640 (11875093, Thermofisher, USA) supplemented with 10% FBS (12103 C, Sigma Aldrich, Shanghai, China), 1% L-glutamine (G7513, Sigma Aldrich, Shanghai, China), 1% penicillin/streptomycin (15140148, Thermofisher, USA), and 15% L929 fibroblast-conditioned medium for 7 days. After differentiation, BMDMs were washed with PBS and resuspended in 5 ml RPMI-1640. Cell scraping was performed, followed by centrifugation at 200 × g for 5 min. The BMDMs were then seeded and stimulated in R10/5 medium (RPMI-1640 supplemented with 10% FBS, 2 mM L-glutamine, 100 U/ml penicillin, 100 μg/ml streptomycin, and 5% LCCM) [76–78]. BMDMs were treated with 500 ng/ml of LPS for three hours [79]. Subsequently, cell viability, levels of inflammatory factors, and oxidative stress were assessed. Macrophage-conditioned medium post LPS treatment was used to culture BMSCs, and mitochondrial signaling was analyzed after treating with 10 μM CCCP for 2 h [80].

Cell viability assessment

After 3D bioprinting, live and dead cells were identified using Calcein AM (ThermoFisher, USA, Product No. C3099) and Propidium Iodide (PI) (innibio, USA, Product No. DN1005-010). Cells were incubated in a medium containing 1 μM Calcein AM at 37 ℃ for 30 min, followed by three washes with PBS. Subsequently, cells were incubated in a medium containing 1 μM PI for 10 min, followed by three washes with PBS. Images were captured using a confocal microscope (Carl Zeiss AG, Germany, Model 880), with each image representing a different field of view. Three independent samples were tested. Cell viability was calculated using ImageJ software (Version 1.8.0) [81].

Additionally, cell viability was assessed according to the manufacturer's instructions for the CCK-8 assay kit (Beyotime, Shanghai, China, Product No. C0041). After 48 h of incubation, cell viability was measured using the CCK-8 method. CCK-8 detection solution (10 μL) was added at each measurement, followed by 4 h of incubation in a CO_2 incubator. Absorbance at 450 nm was then measured using an enzyme-linked immunosorbent assay (ELISA) reader to calculate cell viability [82].

Antioxidant activity determination

DPPH radical was used to assess the antioxidant activity of the scaffolds. Firstly, 4 mg of DPPH (Aldrich, Product No. 300267) was dissolved in 100 ml of methanol solution (Aldrich, Shanghai, China, Product No. 439193). Next, cylindrical scaffolds with dimensions of 10 mm (height) × 10 mm (diameter) were immersed in 4 ml of DPPH solution and subjected to antioxidant reaction at 37 °C. Absorbance at 516 nm was measured to evaluate the antioxidant activity by calculating the DPPH clearance efficiency [83].

Detection of total ROS and mitochondrial ROS

The assessment of ROS was conducted using the green fluorescent dye dichlorodihydrofluorescein diacetate (DCF) (HY-D0940, Abcam, UK). This dye has the ability to enter cells and interact with ROS molecules, forming a fluorescent compound called dichlorodihydrofluorescein (DCFDA). In brief, a stock solution of DCFDA (10 mM) was prepared in methanol and then diluted with culture medium to obtain a working solution of 100 μM. Cells were cultured overnight in a six-well plate with coverslips. On the following day, the cells were treated with H_2O_2 (200 μM) for 24 h. After treatment, coverslips were washed with ice-cold Hank's Balanced Salt Solution (HBSS) (H8264, Sigma Aldrich, Shanghai, China) and incubated with 100 μM DCFDA at 37 °C for 30 min. Following washing, coverslips were mounted onto slides. Fluorescence intensity and ratio of positively stained cells were observed and analyzed using a multiphoton confocal microscope (A1R, Nikon, USA) with a ×100 objective, and ImageJ software was employed for data analysis at specific excitation and emission wavelengths.

For the evaluation of superoxide compounds (SOX) present in the mitochondria, the red dye mito-SOX (M36008, Thermo Fisher, USA) was utilized. THP-P cells (2×10^4) were cultured overnight in a six-well plate with coverslips. On the next day, the cells were treated with H_2O_2 (200 μM) for 24 h. Post-treatment, coverslips were washed with ice-cold 1×PBS and incubated at 37 °C for 30 min with a working solution of 2 μM mito-SOX.

Following a final wash with 1×PBS, coverslips were mounted onto slides. Fluorescence intensity and ratio of positively stained cells were observed and analyzed using a multiphoton confocal microscope (A1R, Nikon, USA) with a ×100 objective. ImageJ software was then used for data analysis at specific excitation and emission wavelengths [84].

Flow cytometry analysis

To identify surface markers of BMSCs, we used the following antibodies: CD44 (ab25064, 1:500, Abcam, USA), CD90 (ab24904, 1:50, Abcam, USA), CD45 (ab210225, 1:500, Abcam, USA), and CD34 (ab23830, 1:500, Abcam, USA). Flow cytometry analysis was performed using an Attune NxT flow cytometer (Thermo Fisher Scientific Inc.) [85]. For the identification of surface markers of BMDMs, we used the F4/80 antibody (ab237332, 1:500, Abcam, USA). Flow cytometry analysis was similarly conducted using the Attune NxT flow cytometer (Thermo Fisher Scientific Inc.) [76]. Cell nuclei were stained using an APC-conjugated anti-F4/80 antibody (1:100, ab105080, Abcam, USA) and Sytox Green (R37109, 1:100, Bioscience, USA). An APC-conjugated mouse IgG2a kappa antibody (ab154434, 1:100, Abcam, USA) was used as an isotype control. All antibodies were incubated on ice and protected from light for 15 min. After incubation, the cells were centrifuged and washed with 500 μL of staining buffer. Flow cytometry was used to identify surface markers of BMDMs, with undifferentiated BMs serving as a control [76–78]. To measure ROS levels, we employed the DCFH2-DA probe (HY-D0940, Abcam, UK, 1 μM, 30 min). Cells were collected, and fluorescent intensity was measured using the Attune NxT flow cytometer (Thermo Fisher Scientific Inc.) [86].

Extraction of macrophage mitochondria

The supernatant from macrophage lysis was centrifuged at 10,000 xg for 10 min at 4 °C to obtain the mitochondrial pellet. The mitochondrial pellet was then resuspended in mitochondrial isolation buffer (MIB) containing 70 mM sucrose, 210 mM mannitol, 5 mM HEPES, 1 mM EGTA, and 0.5% (w/v) fatty acid-free BSA at pH 7.2. Subsequently, the resuspended mitochondria were layered on a 15% Percoll gradient (15% Percoll, 10% sucrose in 2.5 M, 75% MIB) and centrifuged at 21,000 xg for 10 min at 4 °C. Finally, the pellet was washed with MIB at 13,000 xg for 10 min at 4 °C [87].

Mitochondrial transfer experiment

In order to observe mitochondrial transfer, macrophages were incubated in a pre-warmed staining solution containing a MitoTracker Red CMXRos probe (50 nM) for 30 min and then washed three times with neutral PBS to remove the unbound probe. Co-cultivation with labeled BMSCs (using Mitotracker Green) was then performed, and after 24 h of cultivation, images were taken using confocal microscopy. The average fluorescence intensity of received mitochondria in BMSCs was analyzed using FlowJo software.

TSNE clustering analysis and cell annotation

To reduce the dimensionality of the scRNA-Seq dataset, we applied Principal Component Analysis (PCA) to the top 2000 highly variable genes with maximum variance. The first 14 principal components were selected for downstream analysis using the Elbowplot function in the Seurat package. To determine the major cell subgroups, we utilized the FindClusters function in Seurat with the default resolution value (resolution = 0.2). Subsequently, we employed the TSNE algorithm to reduce the dimensionality of the scRNA-Seq sequencing data nonlinearly. Lastly, known cell lineage-specific marker genes were utilized, and cell annotation was performed using the online website CellMarker [88].

Single-cell sequencing analysis

The scRNA-Seq data were processed using the Seurat package (version 3.1) in R software with standard downstream processing. The processing steps involved excluding cells with fewer than 200 detected genes and genes detected in less than 3 cells. Additionally, cells with mitochondrial proportions exceeding 10% were restricted. The data were then normalized using the LogNormalize method [89].

Next, clustering of cells was performed using the FindClusters function, and visualization was conducted using the RunUMAP function. Specific marker genes for cell clusters were identified using the FindMarkers function in the Seurat package. To determine differentially expressed genes (DEGs) specific to a particular cluster, the Wilcoxon rank-sum test was applied to compare cells within that cluster against all other cells. A Bonferroni-corrected p-value of less than 0.05 was used as the cutoff for identifying DEGs with statistical significance. Known cell lineage-specific marker genes were used, and cell markers were annotated using the online website CellMarker [90].

RT-qPCR

Total RNA was extracted from tissues or cells using Trizol reagent (15596026, Invitrogen, USA). The concentration and purity of total RNA at 260/280 nm were determined using NanoDrop LITE (ND-LITE-PR, Thermo Scientific™, Germany). The extracted total RNA was then reverse transcribed into cDNA using the PrimeScript RT reagent Kit with gDNA Eraser (RR047Q, TaKaRa, Japan). Subsequently, the SYBR Green PCR Master Mix reagent (4364344, Applied Biosystems,

USA) and ABI PRISM 7500 Sequence Detection System (Applied Biosystems) were used to perform RT-qPCR for each gene. The primers for each gene were synthesized by TaKaRa (Table S1), with GAPDH serving as the internal reference gene. The relative expression levels of each gene were analyzed using the $2^{-\Delta\Delta Ct}$ method, where △△Ct = (average Ct value of target gene in the experimental group - average Ct value of reference gene in the experimental group) - (average Ct value of target gene in the control group - average Ct value of reference gene in the control group) [91–93]. All RT-qPCR detections were performed in triplicate.

Western blot

Total protein from tissues or cells was extracted using highly efficient RIPA lysis buffer (C0481, Sigma-Aldrich, USA) containing 1% protease inhibitor (ST019-5 mg, Beyotime, Shanghai, China) and 1% phosphatase inhibitor. After 15 min of lysis at 4℃, the samples were centrifuged at 13,000 g for 15 min, and the supernatant was collected. The protein concentration of each sample was determined using the BCA assay kit (23227, TH&Ermo, USA). The protein samples were then quantified based on different concentrations and mixed with a 5x loading buffer (P0015, Beyotime, China). The proteins were separated by polyacrylamide gel electrophoresis and transferred onto a PVDF membrane (IPVH00010, Millipore, Billerica, MA, USA). The membrane was blocked with 5% BSA at room temperature for 1 h, followed by incubation with the following primary antibodies overnight: OPN (ab228748, 45 kDa, 1:2000, Abcam, UK), Runx2 (ab264077, 57 kDa, 1:1000, Abcam, UK), ALP (ab229126, 39 kDa, 1:1000, Abcam, UK), OCN (ab93876, 11 kDa, 1:1000, Abcam, UK). The membrane was then washed three times for 5 min each with TBST and incubated with the appropriate diluted secondary antibodies: HRP-conjugated goat anti-rabbit IgG (1:2000, ab205718, Abcam, UK) or goat anti-mouse IgG (1:2000, ab6789, Abcam, UK) at room temperature for 1.5 h. After incubation, the membrane was washed three times for 5 min each with TBST and developed using the chemiluminescent substrate (NCI4106, Pierce, Rockford, IL, USA). Protein quantification analysis was performed using ImageJ software by calculating the grayscale ratio of each protein to the internal control GAPDH (ab8245, 36 kDa, 1:1000, Abcam, UK) [92]. Each experiment was repeated three times.

Immunofluorescence

Cells or tissues were washed with ice-cold PBS and then fixed with 4% paraformaldehyde (P885233, Macklin, USA) for 15 to 30 min. Subsequently, they were treated with 0.1% Triton (L885651, Macklin, USA) for 15 min. After two PBS washes, samples were incubated with PBS solution containing 15% FBS at 5 °C for 4 min overnight. For staining, cells or tissues were covered with antibodies against TNF-α (ab237353, Alexa Fluor® 488, Abcam, UK; 1:100)/iNOS (ab209027, Alexa Fluor® 647, Abcam, UK; 1:100), CD68 (ab201844, Alexa Fluor® 488, Abcam, UK; 1:250)/iNOS (ab209027, Alexa Fluor® 647, Abcam, UK; 1:100), or CD86 (ab275741, Alexa Fluor® 488, Abcam, UK; 1:100)/CD163 (ab313666, Alexa Fluor® 647, Abcam, UK; 1:100). The samples were then incubated overnight at 4 °C. DAPI staining (D1306, Thermo Fisher, USA) was performed, and observations were made using a fluorescence microscope (Zeiss Observer Z1, Germany). The fluorescent intensity was measured in selected areas, and image processing and quantification were performed using ImageJ software to determine the number of positive cells [94].

ATP measurement

Cellular ATP levels were measured using an ATP assay kit (BC0300, Solarbio, Beijing, China). Cells were lysed by centrifugation to separate cell pellets from culture supernatants. Cell pellets were resuspended in 300 μL of hot double-distilled water, homogenized by heat in a water bath at 95 °C, and further heated in a boiling water bath for 10 min. Next, 30 μL of the sample was mixed with reagents one, two, three, and distilled water following the kit's instructions. After thorough mixing and a 30-minute incubation at 37 °C, 50 μL of reagent four was added, mixed well, and centrifuged at 4000 rpm for 5 min. The supernatant (300 μL) was collected, mixed with 500 μL of reagent five, incubated at room temperature for 2 min, followed by the addition of 500 μL of reagent six and a 5-minute incubation at room temperature. The absorbance was measured at 636 nm with a path length of 0.5 cm using a UV spectrophotometer (DU720, Beckman, USA) [95].

Bioenergetic analysis

Bioenergetic measurements were performed using the Seahorse Bioscience XFe24 Flux Analyzer (Agilent Technologies) following the manufacturer's instructions. Briefly, cells were seeded at a density of 5×10^4 cells per well on a collagen-coated 24-well Seahorse XFe plate overnight. The oxygen consumption rate (OCR) was measured using a basal assay medium containing 1 mM pyruvate, 10 mM glucose, and 2 mM glutamine (25030081, Thermo Fisher, USA). Subsequently, samples were treated with 1 μM oligomycin (ab141829, Abcam, UK), 2 μM FCCP (ab120081, Abcam, UK), and 0.5 μM rotenone/antimycin A (ab52922, Abcam, UK) sequentially. Finally, the measured values were normalized to cell number per well and analyzed using Seahorse Wave software [96].

JC-1 staining

Cells were seeded at a density of 2×10^4 in 35 mm culture dishes and incubated overnight. The following day, cells were treated for 24 h in different experimental groups. Afterward, cells were washed three times with 1×PBS and co-incubated with JC-1 dye (T3168, Thermo Fisher, USA) for 20 min at 37 °C. After washing, cells were mounted on glass slides and observed under a fluorescence microscope. ImageJ software was used for image analysis, statistical analysis, and quantification of the percentage of positive cells [97].

ELISA

Cell or tissue samples to be tested were collected and lysed or centrifuged to obtain supernatants, following the instructions provided with the assay kits. IL-1β ELISA kit (ab197742, Abcam, UK), IL-6 ELISA kit (ab100712, Abcam, UK), and TNF-α ELISA kit (ab208348, Abcam, UK) were used. First, the antigen used was diluted to an appropriate concentration in coating buffer, and 5% bovine serum (F8318, MSK, Wuhan, China) was added to seal the enzyme reaction wells at 37 °C for 40 min. Diluted samples were added to the enzyme reaction wells, followed by the addition of the enzyme conjugate and substrate solution. The reaction was stopped by adding 50μL of stop solution to each well within 20 min. The plate was read at 450 nm using an enzyme reader (Bio-Rad, USA), and a standard curve was plotted. Finally, data analysis was performed [98, 99].

Animal experiments

BALB/c male mice aged 7–8 weeks and weighing 16–20 g were obtained from the Experimental Animal Research Center at our institution. All animal studies were conducted in accordance with our institution's "Guidelines for the Care and Use of Laboratory Animals." The mice were housed at a temperature of 23±1 °C and a relative humidity of 55±5%, with a 12-hour light/dark cycle and free access to food and water. To acclimatize to the environment, the mice were kept under these conditions for 2 to 3 days prior to the experiments [100].

Establishment of a mouse model for femoral fractures

A mouse model for femoral fractures was established using 7-8-week-old male BALB/c mice weighing 16–20 g. The mice were anesthetized with chloral hydrate (50 mg/kg, C8383, Sigma-Aldrich, USA). The leg was cleaned with 10% iodine solution, and a longitudinal incision was made on the skin to expose the femur after separating the muscles. Subsequently, a three-point bending device was used to induce a fracture near the proximal end of the femur, followed by fixation with a 30-gauge intramedullary needle. The incision was closed using 5−0 absorbable sutures, and another fracture was induced using the three-point bending device. After anesthesia recovery, the mice were allowed unrestricted movement without any weight-bearing restrictions. Fractures that were not located in the midshaft or severe comminuted fractures were excluded from the study. Prior to fracture induction, sustained-release buprenorphine (3.25 mg/kg) was administered as an analgesic and repeated every 72 h for a total of 7 days [101].

For the group receiving scaffold treatment for fractures, a printed gel scaffold was placed in the fracture marrow cavity and fixed using a 30-gauge needle after the fracture. Animal experimental groups were as follows:

Normal group: Normal mice without any intervention.

Model group: Mice with fractures treated using natural healing after fixation and suturing.

GA group: Mice with fractures treated using a 3D-printed GA scaffold at the fracture site.

GAD/Ag-pIO group: Mice with fractures treated using a 3D-printed GAD/Ag-pIO scaffold at the fracture site.

GAD/Ag-pIO + mito group: Mice with fractures treated using a 3D-printed GAD/Ag-pIO scaffold loaded with extracted macrophage mitochondria (mito) at the fracture site.

Immunohistochemistry and immunofluorescence observations were conducted on randomly selected six mice from each group on the 3rd, 7th, and 14th days after fracture to observe changes in the inflammatory process during the healing process. Micro-CT was used to observe the growth of newly formed bone at the fracture site on the 14th and 35th days after fracture. On the 35th day after complete fracture healing, bone tissue was stained with H&E, and the mechanical strength of the healing bone was evaluated using a four-point bending mechanical test. Six mice from each group were sampled [101, 102].

Micro-CT analysis

The femoral bone tissue region was scanned using a micro-CT system (mCT-40, Scanco Medical, Switzerland) to investigate the growth characteristics of the femoral bone tissue. The scanning parameters were set as follows: power current: 385μA, power voltage: 65 kV, pixel size: 9 μm, filter: AI 1.0 mm, rotation step: 0.4°. Image reconstruction was performed using Bruker's NRecon software, followed by data analysis using the CTAn program. Two specific volumes of interest were created at a height of 0.5 mm above the growth plate of the femoral head and at a height of 0.25 mm. The region of interest (ROI) beneath the articular cartilage within these volumes was manually defined, and a constant threshold (50–255) was applied for binarization using trabecular bone. The micro-CT parameters analyzed

were as follows: (a) trabecular bone volume fraction (bone volume/total tissue volume, BV/TV): the ratio of bone surface area to tissue volume; (b) trabecular bone thickness (Tb.Th): the average thickness of trabeculae, used to describe trabecular structure changes; (c) trabecular bone number (Tb.N): the number of intersections between bone and non-bone tissues per unit length; (d) bone density (bone mineral density, BMD): the distribution of bone mass and density within the skeleton [103, 104].

Four-point bending mechanical testing

Mechanical testing was conducted on the second day following animal euthanasia at ambient temperature. The contralateral femur was compared to an internal control group. A four-point bending device equipped with a 50 N load cell sensor (Hounsfield Test Equipment Ltd, UK) was employed to assess femoral healing. During the tests, loading was applied along the anteroposterior axis, with an inner span of 8 mm and an outer span of 20 mm. The femur's long axis was maintained perpendicular to the blades. The QMAT Professional software (Tinius Olsen Inc., Horsham, PA, USA) was used to measure and analyze ultimate load (UL), elastic modulus (E-modulus), and failure energy. These biomechanical properties were expressed as percentages relative to the values obtained from the intact contralateral skeleton [105].

Pathology tissue/cell staining

Hematoxylin and Eosin (H&E) Staining: Tissue samples for examination are obtained and subjected to fixation. Paraffin-embedded sections are placed in xylene to remove the wax. Then, they are dehydrated in sequential baths of 100% ethanol, 95% ethanol, and 70% ethanol. Subsequently, the sections can be either embedded or rinsed with water. The prepared sections are stained in hematoxylin staining solution (H8070, Solarbio, Beijing, China) for approximately 5–10 min at room temperature. Afterward, the slides are rinsed with distilled water and dehydrated in 95% ethanol. The sections are then stained with an eosin staining solution (G1100, Solarbio, Beijing, China) for 5–10 min. Finally, standard procedures for dehydration, clearing, and slide coverslipping are followed [106]. ImageJ software is utilized for image processing and quantitative analysis of the newly formed bone area [102, 107].

ALP Staining: ALP detection is performed using an ALP staining kit (CTCC-JD002, Puhui Biotech, Wuxi, China). ALP staining solution is prepared according to the instructions provided. In each 10 mL of the color development buffer, 33 μL of BCIP solution and 66 μL of NBT solution are added. After thorough mixing, an appropriate amount of staining solution is added to each well to cover the cells. The plate is incubated at room temperature in the dark for 30 min. If no blue staining is observed within 30 min, incubation can be continued overnight. After discarding the staining solution, the plate is washed twice with distilled water to stop the reaction. Following the removal of the wash solution, images are captured, and ALP activity is quantitatively analyzed by measuring the optical density [107].

ARS Staining: ARS staining kit (C01383, Yagebio, Shanghai, China) is used for detection. Alizarin Red forms a visible orange-red complex with calcium ions, which is used to identify the presence of calcium nodules. The specific steps are as follows: add an appropriate amount of ARS staining solution to cover the cells and incubate at room temperature for 5 min, during which orange-red clusters can be observed. Discard the staining solution, and wash the plate three times with distilled water to stop the reaction. Images are captured, and quantitative analysis is performed by measuring absorbance values [107].

Immunohistochemistry staining

The tissue or cells to be tested were fixed and embedded. The embedded tissue was then sectioned and subjected to dewaxing treatment to remove the paraffin, making it hydrophilic for subsequent immunostaining procedures. The dewaxed tissue sections were treated with SOD1 protein antibody (ab308181, Abcam, UK, 1:100) and IL-1β protein antibody (ab315084, Abcam, UK, 1:500). The sections were processed with Anti-Rabbit-HRP secondary antibody (12–348, Sigma Aldrich, Shanghai, China, 1:1000). DAPI staining (ab64238, Abcam, USA) was used to visualize the sites where the secondary antibody bound to the primary antibodies. The stained tissue sections were then dewaxed and coverslipped. The sections were observed under a microscope, and Image J software was used for image processing and quantitative analysis of the positive efficiency [108, 109].

Statistical analysis

Statistical analysis was performed using ImageJ, SPSS 25, and GraphPad Prism 8 software. All data were processed using GraphPad Prism 8.0 and presented as mean ± standard deviation (Mean ± SD) for continuous variables. An unpaired t-test was used to compare the two groups, and one-way analysis of variance (ANOVA) was employed for multiple group comparisons. Levene's test was used to test for homogeneity of variance. In the case of homogeneity, Dunnett's t-test and LSD-t-test were used for pairwise comparisons. In the presence of heterogeneity of variance, Dunnett's T3 test was employed. Pearson's correlation analysis was used to determine the correlation between genes and the content of immune cells. A p-value of <0.05 was considered statistically significant for group comparisons [110].

Abbreviations

ROS	Reactive Oxygen Species
BMSCs	Bone Marrow-Derived Mesenchymal Stem Cells
ALP	Alkaline Phosphatase
ARS	Alizarin Red S
DA	Dopamine
Ag-pIO	Iron Oxide-Dopamine-Silver Nanoparticles
TEM	Transmission Electron Microscope
TG	Thermogravimetric Analysis
EDS	Energy Dispersive Spectrometer
SEM	Scanning Electron Microscope
FT-IR	Fourier-Transform Infrared Spectroscopy
ICP-OES	Inductively Coupled Plasma Optical Emission Spectrometry
ELISA	Enzyme-Linked Immunosorbent Assay
DCFH-DA	Dichlorodihydrofluorescein Diacetate
PI	Propidium Iodide
BMDMs	Bone Marrow-Derived Macrophages
LPS	Lipopolysaccharide
TNF-α	Tumor Necrosis Factor Alpha
IL-6	Interleukin 6
IL-1β	Interleukin 1 Beta
DPPH	2,2-Diphenyl-1-picrylhydrazyl
UV	Ultraviolet
MB	Methylene Blue
NAC	N-acetylcysteine
BMPs	Bone Morphogenetic Proteins
VEGF	Vascular Endothelial Growth Factor
TGF-β	Transforming Growth Factor Beta
CCCP	Carbonyl Cyanide m-Chlorophenyl Hydrazone
MTT	Methyl Thiazolyl Tetrazolium
Runx2	Runt-Related Transcription Factor 2
SOD1	Superoxide Dismutase 1

Supplementary Information

The online version contains supplementary material available at https://doi.org/10.1186/s12951-024-02757-1.

Supplementary Material 1

Supplementary Material 2

Supplementary Material 3

Supplementary Material 4

Supplementary Material 5

Supplementary Material 6

Supplementary Material 7

Supplementary Material 8

Supplementary Material 9

Acknowledgements
None.

Author contributions
Shui Qiu and Lili Cao conceived and designed the study. Dingding Xiang, Shu Wang, and Di Wang performed the experiments. Yiyi Qian, Xiaohua Li and Xiaoshu Zhou analyzed the data. Shui Qiu and Lili Cao wrote the manuscript. All authors reviewed and approved the final version of the manuscript.

Funding
This study was supported by Liaoning Provincial Natural Science Foundation (No. 2023-BS-102).

Data availability
No datasets were generated or analysed during the current study.

Declarations

Ethics approval and consent to participate
All animal experiments were approved by the Animal Ethics Committee of IACUC Issue NO. KT20221199.

Consent for publication
Not applicable.

Competing interests
The authors declare no competing interests.

Received: 22 March 2024 / Accepted: 5 August 2024
Published online: 05 September 2024

References

1. Mayo Z, Allen BG, An Q, Miller BJ. Skeletal related events are rare after Radiation Treatment for Metastatic Disease of the Femur. Iowa Orthop J. 2021;41(1):83–7.
2. Straszewski AJ, Schultz K, Dickherber JL, Dahm JS, Wolf JM, Strelzow JA. Gunshot-related Upper extremity nerve injuries at a level 1 Trauma Center. J Hand Surg Am. 2022;47(1):88e. 1-88.e6.
3. Werderman DS. Imaging hip fractures. Radiol Technol. 2022;93(3):279–300.
4. Rickert MM, Windmueller RA, Ortega CA et al. Sacral Insufficiency Fractures. JBJS Rev. 2022;10(7):e22.00005. Published 2022 Jul 8. https://doi.org/10.2106/JBJS.RVW.22.00005
5. Rämö L, Sumrein BO, Lepola V, et al. Effect of surgery vs functional bracing on functional outcome among patients with closed Displaced Humeral Shaft fractures: the FISH randomized clinical trial. JAMA. 2020;323(18):1792–801. https://doi.org/10.1001/jama.2020.3182.
6. Jannin A, Kerlan V, Desailloud R. Endocrinology of bone mineralization: an update. Ann Endocrinol (Paris). 2022;83(1):46–53. https://doi.org/10.1016/j.ando.2021.12.001.
7. Rizkallal C, Lafuente P. Feline skull injuries: treatment goals and recommended approaches. J Feline Med Surg. 2020;22(3):229–40. https://doi.org/10.1177/1098612X20903602.
8. Johansson H, Dela SS, Cassim B et al. FRAX-based fracture probabilities in South Africa. Arch Osteoporos. 2021;16(1):51. Published 2021 Mar 1. https://doi.org/10.1007/s11657-021-00905-w
9. Mollahosseini M, Ahmadirad H, Goujani R, Khorramdelazad H. The Association between Traumatic Brain Injury and Accelerated Fracture Healing: a study on the effects of Growth factors and cytokines. J Mol Neurosci. 2021;71(1):162–8. https://doi.org/10.1007/s12031-020-01640-6.
10. Hassan TAL, Razzaq RMA. Evaluation of the efficacy of Biodegradable plates in Maxillofacial fractures. J Craniofac Surg. 2022;33(4):1166–9. https://doi.org/10.1097/SCS.0000000000008444.
11. Wang Y, Agenor A, Clement A, Hopfgartner A, Whyne C, Nam D, Probiotics. Can it modulate fracture healing? PLoS ONE. 2023;18(8):e0290738. https://doi.org/10.1371/journal.pone.0290738. Published 2023 Aug 31.
12. Barros R, Ribeiro JGA, da Silva HAM, de Sá FR, Fosse AM, Júnior, Favorito LA. Urethral injury in penile fracture: a narrative review. Int Braz J Urol. 2020;46(2):152–7. https://doi.org/10.1590/S1677-5538.IBJU.2020.99.02.
13. Lichaa R, Deeb G, Mhanna R, Zogheib C. Comparison of fracture resistance between single-cone and warm Vertical compaction technique using Bio-C Sealer in Mandibular incisors: an in Vitro Study. J Contemp Dent Pract. 2022;23(2):143–8. Published 2022 Feb 1.
14. Oguzkaya S, Güvercin YS, Kızkapan TB, Eken G, Arat F, Misir A. Fracture lines and comminution zones of traumatic sacral fractures. Sakrum kırıklarının 3 boyutlu haritalandırılması. Ulus Travma Acil Cerrahi Derg. 2023;29(2):247–51. https://doi.org/10.14744/tjtes.2022.15163.
15. Sun K, Jing X, Guo J, Yao X, Guo F. Mitophagy in degenerative joint diseases. Autophagy. 2021;17(9):2082–92. https://doi.org/10.1080/15548627.2020.1822097.
16. Hu Q, Lyon CJ, Fletcher JK, Tang W, Wan M, Hu TY. Extracellular vesicle activities regulating macrophage- and tissue-mediated injury and repair responses. Acta Pharm Sin B. 2021;11(6):1493–512. https://doi.org/10.1016/j.apsb.2020.12.014.
17. Zhang W, Wang N, Yang M, et al. Periosteum and development of the tissue-engineered periosteum for guided bone regeneration. J Orthop Translat.

2022;33:41–54. https://doi.org/10.1016/j.jot.2022.01.002. Published 2022 Feb 16.
18. Wu M, Liu F, Yan L, et al. MiR-145-5p restrains chondrogenic differentiation of synovium-derived mesenchymal stem cells by suppressing TLR4. Nucleosides Nucleotides Nucleic Acids. 2022;41(7):625–42. https://doi.org/10.1080/15257770.2022.2057535.
19. Atmar K, Tulling AJ, Lankester AC, et al. Functional and Immune Modulatory characteristics of bone marrow mesenchymal stromal cells in patients with aplastic Anemia: a systematic review. Front Immunol. 2022;13:859668. https://doi.org/10.3389/fimmu.2022.859668. Published 2022 Mar 9.
20. Li J, Jiang X, Li H, Gelinsky M, Gu Z. Tailoring materials for modulation of macrophage fate. Adv Mater. 2021;33(12):e2004172. https://doi.org/10.1002/adma.202004172.
21. Gauthier T, Chen W. Modulation of macrophage immunometabolism: a New Approach to fight infections. Front Immunol. 2022;13:780839. https://doi.org/10.3389/fimmu.2022.780839. Published 2022 Jan 26.
22. Rao L, Zhao SK, Wen C, et al. Activating macrophage-mediated Cancer Immunotherapy by genetically edited nanoparticles. Adv Mater. 2020;32(47):e2004853. https://doi.org/10.1002/adma.202004853.
23. Cheng K, Zhang H, Guo Q, et al. Emerging trends and research foci of oncolytic virotherapy for central nervous system tumors: a bibliometric study. Front Immunol. 2022;13:975695. https://doi.org/10.3389/fimmu.2022.975695. Published 2022 Sep 6.
24. Manneken JD, Currie PD. Macrophage-stem cell crosstalk: regulation of the stem cell niche. Development. 2023;150(8):dev201510. https://doi.org/10.1242/dev.201510.
25. Borcherding N, Jia W, Giwa R, et al. Dietary lipids inhibit mitochondria transfer to macrophages to divert adipocyte-derived mitochondria into the blood. Cell Metab. 2022;34(10):1499–e15138. https://doi.org/10.1016/j.cmet.2022.08.010.
26. Chen J, Fu CY, Shen G, et al. Macrophages induce cardiomyocyte ferroptosis via mitochondrial transfer. Free Radic Biol Med. 2022;190:1–14. https://doi.org/10.1016/j.freeradbiomed.2022.07.015.
27. Dominguez-Gutierrez PR, Kwenda EP, Khan SR, Canales BK. Immunotherapy for stone disease. Curr Opin Urol. 2020;30(2):183–9. https://doi.org/10.1097/MOU.0000000000000729.
28. Sylwestrak EL, Jo Y, Vesuna S, et al. Cell-type-specific population dynamics of diverse reward computations. Cell. 2022;185(19):3568–e358727. https://doi.org/10.1016/j.cell.2022.08.019.
29. Cong Y, Fu J. Hydrogel-tissue interface interactions for Implantable Flexible Bioelectronics. Langmuir. 2022;38(38):11503–13. https://doi.org/10.1021/acs.langmuir.2c01674.
30. Tian A, Yi X, Sun N. Application of mesenchymal stem cells combined with nano-polypeptide hydrogel in tissue engineering blood vessel. Regen Ther. 2022;21:277–81. https://doi.org/10.1016/j.reth.2022.07.009. Published 2022 Aug 27.
31. Hu S, Wang L, Li J, et al. Catechol-Modified and MnO^2-Nanozyme-Reinforced hydrogel with improved antioxidant and antibacterial capacity for Periodontitis Treatment. ACS Biomater Sci Eng. 2023;9(9):5332–46. https://doi.org/10.1021/acsbiomaterials.3c00454.
32. Zha Z, Chen Q, Xiao D, et al. Mussel-inspired Microgel Encapsulated NLRP3 inhibitor as a synergistic strategy against Dry Eye. Front Bioeng Biotechnol. 2022;10:913648. https://doi.org/10.3389/fbioe.2022.913648. Published 2022 Jun 1.
33. Mu S, Guo S, Wang X, et al. Effects of deferoxamine on the osteogenic differentiation of human periodontal ligament cells. Mol Med Rep. 2017;16(6):9579–86. https://doi.org/10.3892/mmr.2017.7810.
34. Beňačka R, Szabóová D, Guľašová Z, Hertelyová Z, Radoňák J. Classic and New Markers in Diagnostics and classification of breast Cancer. Cancers (Basel). 2022;14(21):5444. https://doi.org/10.3390/cancers14215444. Published 2022 Nov 5.
35. Bharadwaz A, Jayasuriya AC. Recent trends in the application of widely used natural and synthetic polymer nanocomposites in bone tissue regeneration. Mater Sci Eng C Mater Biol Appl. 2020;110:110698. https://doi.org/10.1016/j.msec.2020.110698.
36. Shang A, Gu C, Wang W et al. Exosomal circPACRGL promotes progression of colorectal cancer via the miR-142-3p/miR-506-3p- TGF-β1 axis. Mol Cancer. 2020;19(1):117. Published 2020 Jul 27. https://doi.org/10.1186/s12943-020-01235-0
37. Sukhorukova IV, Sheveyko AN, Shvindina NV, Denisenko EA, Ignatov SG, Shtansky DV. Approaches for controlled Ag^+ ion release: influence of Surface Topography, Roughness, and Bactericide Content. ACS Appl Mater Interfaces. 2017;9(4):4259–71. https://doi.org/10.1021/acsami.6b15096.
38. Yasue H, Obata K, Okumura K, et al. Increased secretion of atrial natriuretic polypeptide from the left ventricle in patients with dilated cardiomyopathy. J Clin Invest. 1989;83(1):46–51. https://doi.org/10.1172/JCI113883.
39. Liu C, Yang B, Chen J, Jia F, Song S. Synergetic degradation of Methylene Blue through photocatalysis and Fenton reaction on two-dimensional molybdenite-Fe. J Environ Sci (China). 2022;111:11–23. https://doi.org/10.1016/j.jes.2021.03.001.
40. Hu K, Shang Z, Yang X, Zhang Y, Cao L. Macrophage polarization and the regulation of bone immunity in bone homeostasis. J Inflamm Res. 2023;16:3563–80. https://doi.org/10.2147/JIR.S423819. Published 2023 Aug 22.
41. Wu M, Chen G, Li YP. TGF-β and BMP signaling in osteoblast, skeletal development, and bone formation, homeostasis and disease. Bone Res. 2016;4:16009. https://doi.org/10.1038/boneres.2016.9. Published 2016 Apr 26.
42. Fan S, Sun X, Su C, Xue Y, Song X, Deng R. Macrophages-bone marrow mesenchymal stem cells crosstalk in bone healing. Front Cell Dev Biol. 2023;11:1193765. https://doi.org/10.3389/fcell.2023.1193765. Published 2023 Jun 23.
43. Jain A, Zoncu R. Organelle transporters and inter-organelle communication as drivers of metabolic regulation and cellular homeostasis. Mol Metab. 2022;60:101481. https://doi.org/10.1016/j.molmet.2022.101481.
44. Borcherding N, Brestoff JR. The power and potential of mitochondria transfer. Nature. 2023;623(7986):283–91. https://doi.org/10.1038/s41586-023-06537-z.
45. Zhou M, Yu Y, Luo X, et al. Myocardial ischemia-reperfusion Injury: therapeutics from a Mitochondria-Centric Perspective. Cardiology. 2021;146(6):781–92. https://doi.org/10.1159/000518879.
46. Ikeda G, Santoso MR, Tada Y, et al. Mitochondria-Rich Extracellular vesicles from autologous stem cell-derived cardiomyocytes restore energetics of ischemic myocardium. J Am Coll Cardiol. 2021;77(8):1073–88. https://doi.org/10.1016/j.jacc.2020.12.060.
47. Su YJ, Wang PW, Weng SW. The Role of Mitochondria in Immune-Cell-Mediated Tissue Regeneration and Ageing. Int J Mol Sci. 2021;22(5):2668. Published 2021 Mar 6. https://doi.org/10.3390/ijms22052668
48. Porubska B, Vasek D, Somova V, et al. Sertoli Cells Possess Immunomodulatory Properties and the ability of mitochondrial transfer similar to mesenchymal stromal cells. Stem Cell Rev Rep. 2021;17(5):1905–16. https://doi.org/10.1007/s12015-021-10197-9.
49. Shimoni C, Goldstein M, Ribarski-Chorev I, et al. Heat shock alters mesenchymal stem cell identity and induces premature senescence. Front Cell Dev Biol. 2020;8:565970. https://doi.org/10.3389/fcell.2020.565970. Published 2020 Sep 22.
50. Wang JG, Zhao XG, Wang XL, Liu MX, Wan W. Low expression of miR-1 promotes osteogenic repair of bone marrow mesenchymal stem cells by targeting TLR1. Eur Rev Med Pharmacol Sci. 2020;24(7):3492–500. https://doi.org/10.26355/eurrev_202004_20808.
51. Zhang W, Hou W, Chen M, et al. Upregulation of parkin accelerates osteoblastic differentiation of bone marrow-derived mesenchymal stem cells and bone regeneration by enhancing autophagy and β-Catenin signaling. Front Cell Dev Biol. 2020;8:576104. https://doi.org/10.3389/fcell.2020.576104. Published 2020 Sep 15.
52. Saul D, Khosla S. Fracture Healing in the setting of Endocrine diseases, Aging, and Cellular Senescence. Endocr Rev. 2022;43(6):984–1002. https://doi.org/10.1210/endrev/bnac008.
53. Libby P. Inflammation during the life cycle of the atherosclerotic plaque. Cardiovasc Res. 2021;117(13):2525–36. https://doi.org/10.1093/cvr/cvab303.
54. Wang Y, Lin Q, Zhang H, et al. M2 macrophage-derived exosomes promote diabetic fracture healing by acting as an immunomodulator. Bioact Mater. 2023;28:273–83. https://doi.org/10.1016/j.bioactmat.2023.05.018. Published 2023 Jun 1.
55. Ji X, Yuan X, Ma L, et al. Mesenchymal stem cell-loaded thermosensitive hydroxypropyl chitin hydrogel combined with a three-dimensional-printed poly(ε-caprolactone) /nano-hydroxyapatite scaffold to repair bone defects via osteogenesis, angiogenesis and immunomodulation. Theranostics. 2020;10(2):725–40. https://doi.org/10.7150/thno.39167. Published 2020 Jan 1.
56. Benayahu D, Pomeraniec L, Shemesh S, et al. Biocompatibility of a Marine collagen-based Scaffold in Vitro and in vivo. Mar Drugs. 2020;18(8):420. https://doi.org/10.3390/md18080420. Published 2020 Aug 11.
57. Chen LL, Morcelle C, Cheng ZL, et al. Itaconate inhibits TET DNA dioxygenases to dampen inflammatory responses. Nat Cell Biol. 2022;24(3):353–63. https://doi.org/10.1038/s41556-022-00853-8.

58. Lan Y, Yeung TL, Huang H, et al. Colocalized targeting of TGF-β and PD-L1 by bintrafusp alfa elicits distinct antitumor responses. J Immunother Cancer. 2022;10(7):e004122. https://doi.org/10.1136/jitc-2021-004122.
59. Turton KB, Ingram RJ, Valvano MA. Macrophage dysfunction in cystic fibrosis: nature or nurture? J Leukoc Biol. 2021;109(3):573–82. https://doi.org/10.1002/JLB.4RU0620-245R.
60. Fang J, Ou Q, Wu B, et al. TcpC inhibits M1 but promotes M2 macrophage polarization via regulation of the MAPK/NF-κB and Akt/STAT6 pathways in urinary tract infection. Cells. 2022;11(17):2674. https://doi.org/10.3390/cells11172674. Published 2022 Aug 28.
61. Fan N, Zhang X, Zhao W, et al. Covalent inhibition of pyruvate kinase M2 reprograms metabolic and inflammatory pathways in hepatic macrophages against non-alcoholic fatty liver disease. Int J Biol Sci. 2022;18(14):5260–75. https://doi.org/10.7150/ijbs.73890. Published 2022 Aug 15.
62. Chen S, Chen L, Ye L, et al. PP2A-mTOR-p70S6K/4E-BP1 axis regulates M1 polarization of pulmonary macrophages and promotes ambient particulate matter induced mouse lung injury. J Hazard Mater. 2022;424(Pt C):127624. https://doi.org/10.1016/j.jhazmat.2021.127624.
63. Cowan AJ, Green DJ, Kwok M, et al. Diagnosis and management of multiple myeloma: a review. JAMA. 2022;327(5):464–77. https://doi.org/10.1001/jama.2022.0003.
64. Carleton MM, Sefton MV. Promoting endogenous repair of skeletal muscle using regenerative biomaterials. J Biomed Mater Res A. 2021;109(12):2720–39. https://doi.org/10.1002/jbm.a.37239.
65. Galván Morales MA, Barrera Rodríguez R, Santiago Cruz JR, Teran LM. Overview of new treatments with immunotherapy for breast Cancer and a proposal of a combination therapy. Molecules. 2020;25(23):5686. https://doi.org/10.3390/molecules25235686. Published 2020 Dec 2.
66. Zhang R, Xia Y, Wang Z, et al. Serum long non coding RNA MALAT-1 protected by exosomes is up-regulated and promotes cell proliferation and migration in non-small cell lung cancer. Biochem Biophys Res Commun. 2017;490(2):406–14. https://doi.org/10.1016/j.bbrc.2017.06.055.
67. Zou Y, Chen X, Yang P, et al. Regulating the absorption spectrum of polydopamine. Sci Adv. 2020;6(36):eabb4696. https://doi.org/10.1126/sciadv.abb4696. Published 2020 Sep 4.
68. Dong H, Li Z, Bian S, et al. Culture of patient-derived multicellular clusters in suspended hydrogel capsules for pre-clinical personalized drug screening. Bioact Mater. 2022;18:164–77. https://doi.org/10.1016/j.bioactmat.2022.03.020. Published 2022 Mar 19.
69. Lee C, Shin J, Lee JS, et al. Bioinspired, calcium-free alginate hydrogels with tunable physical and mechanical properties and improved biocompatibility. Biomacromolecules. 2013;14(6):2004–13. https://doi.org/10.1021/bm400352d.
70. Mao S, Ren Y, Chen S, Liu D, Ye X, Tian J. Development and characterization of pH responsive sodium alginate hydrogel containing metal-phenolic network for anthocyanin delivery. Carbohydr Polym. 2023;320:121234. https://doi.org/10.1016/j.carbpol.2023.121234.
71. Ha DH, Chae S, Lee JY, et al. Therapeutic effect of decellularized extracellular matrix-based hydrogel for radiation esophagitis by 3D printed esophageal stent. Biomaterials. 2021;266:120477. https://doi.org/10.1016/j.biomaterials.2020.120477.
72. Gao J, Li M, Cheng J et al. 3D-Printed GelMA/PEGDA/F127DA Scaffolds for Bone Regeneration. J Funct Biomater. 2023;14(2):96. Published 2023 Feb 9. https://doi.org/10.3390/jfb14020096
73. Huang Y, Zhang X, Zhan J, et al. Bone marrow mesenchymal stem cell-derived exosomal miR-206 promotes osteoblast proliferation and differentiation in osteoarthritis by reducing Elf3. J Cell Mol Med. 2021;25(16):7734–45. https://doi.org/10.1111/jcmm.16654.
74. Greggi C, Cariati I, Onorato F, Iundusi R, Scimeca M, Tarantino U. PTX3 effects on osteogenic differentiation in osteoporosis: an in Vitro Study. Int J Mol Sci. 2021;22(11):5944. https://doi.org/10.3390/ijms22115944. Published 2021 May 31.
75. Ha CZ, Chen HY, Wang J, et al. Effect of diabetic osteoblasts on osteogenic differentiation of human umbilical cord mesenchymal stem cells. Biomed Pap Med Fac Univ Palacky Olomouc Czech Repub. 2015;159(3):388–93. https://doi.org/10.5507/bp.2014.007.
76. Drab D, Santocki M, Opydo M, Kolaczkowska E. Impact of endogenous and exogenous nitrogen species on macrophage extracellular trap (MET) formation by bone marrow-derived macrophages. Cell Tissue Res. 2023;394(2):361–77. https://doi.org/10.1007/s00441-023-03832-z.
77. Fei F, Lee KM, McCarry BE, Bowdish DM. Age-associated metabolic dysregulation in bone marrow-derived macrophages stimulated with lipopolysaccharide. Sci Rep. 2016;6:22637. https://doi.org/10.1038/srep22637. Published 2016 Mar 4.
78. Gonçalves R, Kaliff Teófilo Murta G, Aparecida de Souza I, Mosser DM. Isolation and Culture of Bone Marrow-Derived Macrophages from Mice. J Vis Exp. 2023;(196):10.3791/64566. Published 2023 Jun 23. https://doi.org/10.3791/64566
79. Bai D, Du J, Bu X, et al. ALDOA maintains NLRP3 inflammasome activation by controlling AMPK activation. Autophagy. 2022;18(7):1673–93. https://doi.org/10.1080/15548627.2021.1997051.
80. Song Y, Ge X, Chen Y, et al. Mycobacterium bovis induces mitophagy to suppress host xenophagy for its intracellular survival. Autophagy. 2022;18(6):1401–15. https://doi.org/10.1080/15548627.2021.1987671.
81. Liu X, Hao M, Chen Z, et al. 3D bioprinted neural tissue constructs for spinal cord injury repair. Biomaterials. 2021;272:120771. https://doi.org/10.1016/j.biomaterials.2021.120771.
82. Lee D, Kim N, Jeon SH et al. Hesperidin Improves Memory Function by Enhancing Neurogenesis in a Mouse Model of Alzheimer's Disease. Nutrients. 2022;14(15):3125. Published 2022 Jul 29. https://doi.org/10.3390/nu14153125
83. Li Y, Yang L, Hou Y, et al. Polydopamine-mediated graphene oxide and nanohydroxyapatite-incorporated conductive scaffold with an immunomodulatory ability accelerates periodontal bone regeneration in diabetes. Bioact Mater. 2022;18:213–27. https://doi.org/10.1016/j.bioactmat.2022.03.021. Published 2022 Mar 22.
84. Maity J, Barthels D, Sarkar J, et al. Ferutinin induces osteoblast differentiation of DPSCs via induction of KLF2 and autophagy/mitophagy. Cell Death Dis. 2022;13(5):452. https://doi.org/10.1038/s41419-022-04903-9. Published 2022 May 12.
85. Luo Z, Sun Y, Qi B, et al. Human bone marrow mesenchymal stem cell-derived extracellular vesicles inhibit shoulder stiffness via let-7a/Tgfbr1 axis. Bioact Mater. 2022;17:344–59. https://doi.org/10.1016/j.bioactmat.2022.01.016. Published 2022 Jan 23.
86. Yuan R, Li Y, Han S, et al. Fe-Curcumin nanozyme-mediated reactive oxygen species scavenging and anti-inflammation for Acute Lung Injury. ACS Cent Sci. 2022;8(1):10–21. https://doi.org/10.1021/acscentsci.1c00866.
87. Jin P, Pan Q, Lin Y, et al. Platelets facilitate Wound Healing by mitochondrial transfer and reducing oxidative stress in endothelial cells. Oxid Med Cell Longev. 2023;2023:2345279. https://doi.org/10.1155/2023/2345279. Published 2023 Feb 20.
88. Shao X, Liao J, Lu X, Xue R, Ai N, Fan X. scCATCH: automatic annotation on cell types of clusters from single-cell RNA sequencing data. iScience. 2020;23(3):100882. https://doi.org/10.1016/j.isci.2020.100882.
89. Zheng H, Liu H, Ge Y, Wang X. Integrated single-cell and bulk RNA sequencing analysis identifies a cancer associated fibroblast-related signature for predicting prognosis and therapeutic responses in colorectal cancer. Cancer Cell Int. 2021;21(1):552. https://doi.org/10.1186/s12935-021-02252-9. Published 2021 Oct 20.
90. Yan T, Qiu W, Weng H, Fan Y, Zhou G, Yang Z. Single-Cell Transcriptomic Analysis of Ecosystems in Papillary Thyroid Carcinoma Progression. Front Endocrinol (Lausanne). 2021;12:729565. Published 2021 Nov 1. https://doi.org/10.3389/fendo.2021.729565
91. Ayuk SM, Abrahamse H, Houreld NN. The role of photobiomodulation on gene expression of cell adhesion molecules in diabetic wounded fibroblasts in vitro. J Photochem Photobiol B. 2016;161:368–74. https://doi.org/10.1016/j.jphotobiol.2016.05.027.
92. Wu Q, Yi X. Down-regulation of long noncoding RNA MALAT1 protects hippocampal neurons against excessive autophagy and apoptosis via the PI3K/Akt Signaling Pathway in rats with Epilepsy. J Mol Neurosci. 2018;65(2):234–45. https://doi.org/10.1007/s12031-018-1093-3.
93. Mao Q, Liang XL, Zhang CL, Pang YH, Lu YX. LncRNA KLF3-AS1 in human mesenchymal stem cell-derived exosomes ameliorates pyroptosis of cardiomyocytes and myocardial infarction through miR-138-5p/Sirt1 axis. Stem Cell Res Ther. 2019;10(1):393. https://doi.org/10.1186/s13287-019-1522-4. Published 2019 Dec 17.
94. Li W, Zhang S, Liu J, Liu Y, Liang Q. Vitamin K2 stimulates MC3T3–E1 osteoblast differentiation and mineralization through autophagy induction. Mol Med Rep. 2019;19(5):3676–84. https://doi.org/10.3892/mmr.2019.10040.
95. Guo Y, Jia X, Cui Y, et al. Sirt3-mediated mitophagy regulates AGEs-induced BMSCs senescence and senile osteoporosis. Redox Biol. 2021;41:101915. https://doi.org/10.1016/j.redox.2021.101915.
96. Liu X, Yan Z, Cai J, et al. Glucose- and glutamine-dependent bioenergetics sensitize bone mechanoresponse after unloading by modulating

osteocyte calcium dynamics. J Clin Invest. 2023;133(3):e164508. https://doi.org/10.1172/JCI164508. Published 2023 Feb 1.
97. Wu C, Shen Z, Lu Y, Sun F, Shi H. p53 promotes ferroptosis in Macrophages treated with Fe^3O^4 nanoparticles. ACS Appl Mater Interfaces. 2022;14(38):42791–803. https://doi.org/10.1021/acsami.2c00707.
98. Zhang Y, Ning C, Zhou H, Yan Y, Liu F, Huang Y, Interleukin-1β. interleukin-6, and interleukin-17A as indicators reflecting clinical response to celecoxib in ankylosing spondylitis patients. Ir J Med Sci. 2021;190(2):631–8. https://doi.org/10.1007/s11845-020-02366-5.
99. Wu HY, Liu K, Zhang JL. LINC00240/miR-155 axis regulates function of trophoblasts and M2 macrophage polarization via modulating oxidative stress-induced pyroptosis in preeclampsia. Mol Med. 2022;28(1):119. Published 2022 Sep 24. https://doi.org/10.1186/s10020-022-00531-3
100. Li WY, Xiong H, Zhongguo. Gu Shang. 2022;35(4):367–74. https://doi.org/10.12200/j.issn.1003-0034.2022.04.014.
101. Ding Z, Qiu M, Alharbi MA, et al. FOXO1 expression in chondrocytes modulates cartilage production and removal in fracture healing. Bone. 2021;148:115905. https://doi.org/10.1016/j.bone.2021.115905.
102. Pan S, Yin Z, Shi C, et al. Multifunctional Injectable Hydrogel Microparticles loaded with miR-29a abundant BMSCs derived exosomes enhanced bone regeneration by regulating Osteogenesis and Angiogenesis. Small. 2024;20(16):e2306721. https://doi.org/10.1002/smll.202306721.
103. Liu GY, Cao GL, Tian FM, et al. Parathyroid hormone (1–34) promotes fracture healing in ovariectomized rats with type 2 diabetes mellitus. Osteoporos Int. 2017;28(10):3043–53. https://doi.org/10.1007/s00198-017-4148-3.
104. Zuo R, Kong L, Wang M et al. Exosomes derived from human $CD34^+$ stem cells transfected with miR-26a prevent glucocorticoid-induced osteonecrosis of the femoral head by promoting angiogenesis and osteogenesis. Stem Cell Res Ther. 2019;10(1):321. Published 2019 Nov 15. https://doi.org/10.1186/s13287-019-1426-3
105. Kim MS, Chung HJ, Kim KI. Optimal concentration of mesenchymal stem cells for fracture healing in a rat model with long bone fracture. World J Stem Cells. 2022;14(12):839–50. https://doi.org/10.4252/wjsc.v14.i12.839.
106. Bian J, Cai F, Chen H, et al. Modulation of local overactive inflammation via Injectable Hydrogel Microspheres. Nano Lett. 2021;21(6):2690–8. https://doi.org/10.1021/acs.nanolett.0c04713.
107. Li SD, Xing W, Wang SC, et al. Fibulin2: a negative regulator of BMSC osteogenic differentiation in infected bone fracture healing. Exp Mol Med. 2023;55(2):443–56. https://doi.org/10.1038/s12276-023-00942-0.
108. Yang X, Ma Y, Wang X, et al. A 3D-Bioprinted functional Module based on decellularized Extracellular Matrix Bioink for Periodontal Regeneration. Adv Sci (Weinh). 2023;10(5):e2205041. https://doi.org/10.1002/advs.202205041.
109. Alhabbal A, Abou Khamis I. Immunohistochemical analysis of intestinal biopsies in individuals with celiac disease. JGH Open. 2022;6(10):692–5. https://doi.org/10.1002/jgh3.12807. Published 2022 Aug 26.
110. Zhang QF, Li J, Jiang K, et al. CDK4/6 inhibition promotes immune infiltration in ovarian cancer and synergizes with PD-1 blockade in a B cell-dependent manner. Theranostics. 2020;10(23):10619–33. https://doi.org/10.7150/thno.44871. Published 2020 Aug 25.

Publisher's Note